BUOYANCY STORMS IN A ZONAL STREAM EXPERIMENTS WITH ALTIMETRY

YI SUI

Buoyancy Storms in a Zonal Stream

Experiments with Altimetry

by

Yi Sui

A thesis submitted to the
School of Graduate Studies
in partial fulfillment of the
requirements for the degree of
Master of Science

Department of Physics and Physical Oceanography
Memorial University of Newfoundland

September 2013

St. John's Newfoundland

Abstract

This thesis investigates a great storm on Saturn, which was generated by an upwelling source and affected by Saturn's permanent winds. A laboratory model is used to simulate the great storm.

The model was built on a rotating tank filled with water. In a series of experiments, the turbulent flow generated by localized heating is studied in the presence of a background zonal current. The flow is in the form of a β-plume, which consists of clockwise circulations and usually stretches to the west. However, when a strong eastward background zonal current is induced, the plume can be overwhelmed by the current and transports eastward. The experiments demonstrate that the westward-transport velocity inside the plume is proportional to the strength of the source in agreement with linear theory. By separately changing the strength of heating and the intensity of the sink, a regime diagram is obtained, showing the possible space where a β-plume exist. In this study, the Altimetric Imaging Velocimetry (AIV) method is used for measuring the dynamic flow fields.

Acknowledgement

The experience in Memorial University over the past two years was very special for me. It is the first time that I stayed in a foreign country for a long time. Here, people have different languages, different food, and totally different lifestyles. The experience expanded my horizons and will become a valuable memory in my life. I especially want to thank my supervisor, Dr. Yakov Afanasyev, who gave me the chance to pursue my Master degree. I also want to thank my parents who gave me financial support and moral boosting to complete my degree especially living far away from my home town.

In the process of composing this thesis, I read many interesting research papers and reports and have gained a lot of knowledge. I would also like to thank my friend Tristan Hauser and Yang Zhang who gave me so many ideas after reading my drafts. This thesis could not be accomplished without their helps.

Table of Contents

List of Figures

Nomenclature

A_0 – the area of the heater

α – the water thermal expansion coefficient

α_{mn} – the n^{th} root of the Bessel function of the m^{th} order

B_0 – buoyancy flux per unit area

β – beta, used to describe the experimental β parameter

C_p – the heat capacity

c_{gx} – the group velocity of zonal Rossby waves

D_v – the diameter of the baroclinic vortices

E_k – the Ekman number

F – buoyancy flux

f – $f_0 = 2\Omega$ is the experimental Coriolis parameter for the rotating tank

g' – reduced gravity

H_0 – the mean water depth in the tank

h_1 – the thickness of layer for warm water spreads in the horizontal direction

k – the wavenumbers in *x* directions

l – the wavenumbers in *y* directions

Δρ – the density difference between the parcel and the ambient fluid

ρ_a – the density of the ambient fluid

Q – Fluid source

Q_m – the mass flux induced by the heater

Q_h – the heat flux induced by the heater

Q_{mn} – the Fourier-Bessel transform for the source Q

Q_v – volume flux Q_v induced by the heater

R_d – the barotropic radius of deformation

Ro – the Rossby number

Ro_f – the Rossby number at the transition thickness

Ro_{β} – the Froude/Rossby number

γ – polar β-plane

ΔT – the density difference between the parcel and the ambient fluid

U_{east} – the peak values of the east velocity of the background flow

U_{west} – the peak values of the westward velocity of the background flow

U_{rr} – the second derivative of the azimuthal velocity along the radius

U_{plume} – the westward propagation of the β-plume

V – the volume flux V of an eastward zonal flow

V_g – geostrophic velocity

V_a – ageostrophic velocity

W_v – the upward speed of propagating of the quasi-2D vortices

$\mathrm{Z_m}$ – the thickness of the transition layer generated by buoyancy flux

Z_t – the thickness of the turbulent layer generated by buoyancy flux

η – the surface elevation of the water in the tank

$\vec{k}$ – the vertical unit vector

μ – the kinematic viscosity of the water

Chapter 1: Introduction

1.1 Observations of GWS on the Saturn

A great convective storm known as Great White Spots (GWS) was detected at approximately 37.7°N on Saturn, on 5 December 2010. The primal storm, visible as a small white spot grew rapidly in size, expanding from a length of 3,000 km to 8,000 km in just one week (A. Sanchez-Lavega et al., 2011). Following this expansion, the primal storm took on a bow shape, such that two storm tails on the northern and southern flank of the storm stretched eastward and a bright compact spot ('storm head') transported westward. Two months later, the planet was surrounded by two eastward spreading storm tails; one of them was at 35°N and the other one was at 43°N (G. Fischer et al., 2011).

The GWS occurred at time interval of roughly 30 Earth years. In the past 150 years, five similar GWS have been documented. Some particular features make this GWS, which happened on 5 Dec 2010, special. It has a much larger size (approximately five times) and stronger intensity than those previously observed. At this time, a large amount of data has been recorded by ground-based telescopes and the Saturn-orbiting Cassini spacecraft, which provide us with unprecedented observational resources (Read, 2011).

Even though the exact mechanism of GWS is still a mystery, observations and numerical modeling (Sa´nchez-Lavega, 2011) have given some clues that GWS are produced by a buoyancy source such as the upwelling warm, moist air and ammonia from deep water clouds by the convective plume (Fig. 1). These materials then reached the troposphere and formed a great storm. As shown in Fig. 1, the bright and white materials expanded horizontally after being upwelled to the troposphere. Then, the north and south part entrained into strong cloud-top eastward jets and formed two storm tails located respectively at 35°N and 43°N.

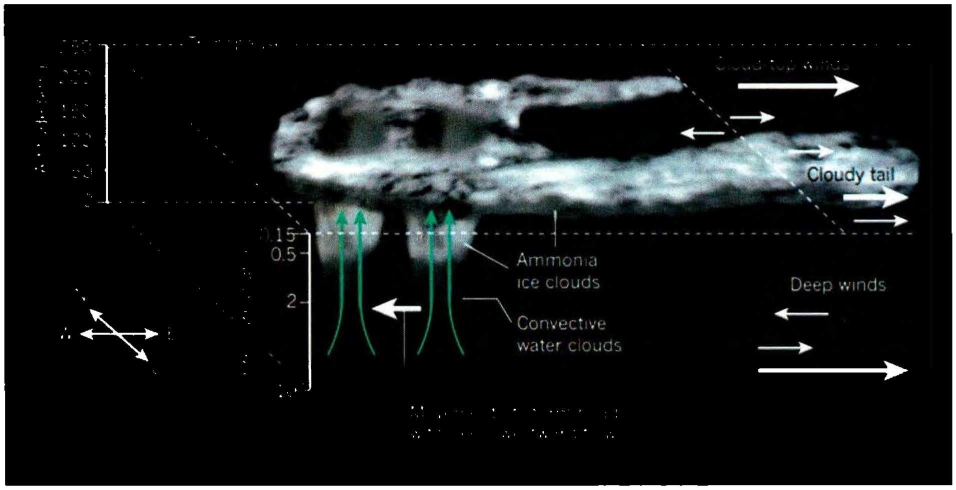

Fig.1 Schematic of the Great White Storm on Saturn of 2010. (Read 2012)

In this GWS event, the source, which was the storm head located at 41°N, moved westward with its highest velocity -28.7 m/s (Sa´nchez-Lavega et al., 2011). Fig. 2 shows a profile of the zonal wind on Saturn, derived from tracking cloud features in Voyager images by Saturn's rotation period from its atmospheric planetary-wave configuration (Read et al., 2009). The wind at the upper cloud level on Saturn remained essentially unchanged throughout a whole Saturn year, and was not altered by the disturbance at the early stage of GWS as observed by Sa´nchez-Lavega et al., (2011). Here, two eastward storm tails correspond to the strong eastward winds at 35°N and 43°N (shown as dot lines in Fig. 2). However, the mean velocity of westward wind at the latitude 41°N where the storm head located was observed as approximately -10 m/s, which is much less than the moving rate of storm head -28.7 m/s (shown by the blue dot in Fig. 2). In addition, the storm head even moved with a speed 10 m/s faster than the peak westward zonal wind (-18 m/s) at 39°N. The differences mean that the westward zonal wind is not enough to explain why the storm head propagates westward. We assume that the second mechanism involved is the β-plume which results from the upwelled materials. The β-plume is a westward stretching quasi-zonal circulation that originates from a continuous source of perturbation on the β-plane (or γ-plane). On Saturn, the upwelled materials played a role as the continuous buoyancy source and created the westward propagating beta-plumes with its front observed as a storm head. Therefore, we conclude that the bow shape of the GWS is due to the combination effects of the background zonal wind and the β-plume. The theory and the mechanisms of β-plume will be described in section 1.3.

This study tried to understand some mechanisms that relate to the formation of the GWS. The experiments were performed in a rotating cylindrical tank filled with water. In the experiments, a continuous buoyancy source and a background zonal flow are introduced on the topographic beta-plane. This paper will focus on showing the dynamics of flows induced by the buoyancy source, the β-plume dynamics and the development of β-plume in the presence of a background zonal current.

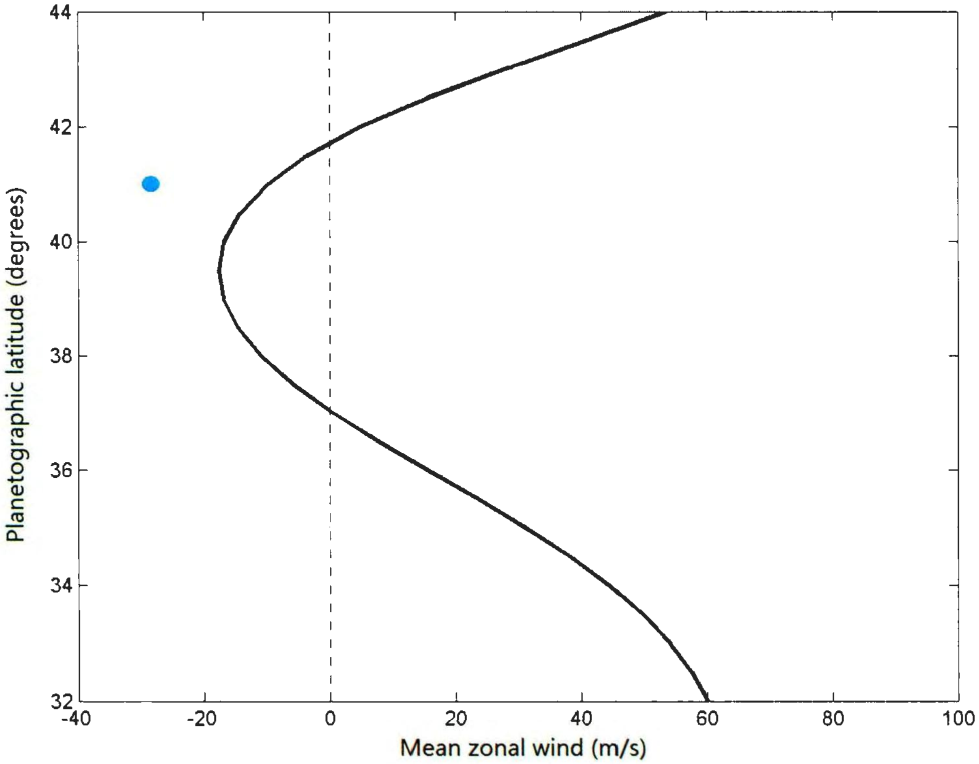

Fig.2 Profile of the mean zonal wind on Saturn, which derived from tracking cloud features in Voyager images by Sa´nchez-Lavega et al. (2000). The blue dot shows the moving rate and the latitude of the storm head.

1.2 Buoyancy Source & Buoyancy Flux

As we described in section 1.1, the GWS was generated by a continuous buoyancy source. In this section, the definition of buoyancy and buoyancy flux will be introduced. In the ocean, the buoyancy source could come in several forms: the heat from a submarine volcano, surface cooling, or evaporation and precipitation, which change salinity or temperature and the density of the water (Cronin and Sprintall, 2001). As heat flux is used to define the rate of heat energy transfer through a given surface, buoyancy flux is used to define the strength of a buoyancy source. In the ocean, buoyancy flux can affect the stability of the upper ocean. The surface cooling or evaporation tends to make the surface water less buoyant and make the water sink, which creates an unstable condition. However, heating or precipitation, which makes the surface water more buoyant by reducing the density, usually contributes to a stable condition (Anitha and Ravichandran, 2006).

Buoyancy force is a force formed by local density differences in a fluid. When a parcel of fluid has a smaller density than its ambient surrounding, the buoyancy force acts as a reduced gravity g' on the parcel and has a positive force direction that moves upward,

$$g' = g\frac{\Delta\rho}{\rho_a}. \qquad (1.1)$$

Here, ρ_0 is the density of the ambient fluid, $\Delta\rho = \rho_0 - \rho_a$ is the density difference between the parcel and the ambient fluid. If $\rho_0 > \rho_a$, the buoyancy force is directed downward. The density difference of the parcel can be expressed by temperature difference, as

$$\Delta\rho = \alpha g \Delta T. \qquad (1.2)$$

Here, α is the water thermal expansion coefficient, ΔT is the temperature difference between the parcel and the ambient fluid assuming temperature change are small.

Assuming the temperature difference ΔT is generated by a localized heater flux (the density difference can be also generated by salinity flux),

$$\Delta T = Q_h / Q_m C_p. \tag{1.3}$$

Here, Q_m is the mass flux induced by the heater, C_p is the heat capacity. After substitute the equation (1.1-1.3) into the original buoyancy flux $F = Q_v g'$, a product by the volume flux Q_v and the reduced buoyancy g'.

We get a common definition of buoyancy flux as follows:

$$F = \frac{\alpha g}{\rho_0 C_p} Q_h \,, \tag{1.4}$$

where α is the water thermal expansion coefficient, g is the gravitational acceleration, ρ_0 is the density of the ambient fluid, C_p is the heat capacity, and Q_h is the heat flux of the heat source. The buoyancy flux of each experiment was computed and shown in Table (2).

1.3 The β-plume Mechanism

Spatial localized perturbations which can be associated with buoyancy sources or sinks often occur in both atmospheres and oceans. These perturbations such as cooling/heating, mass exchanging (coastal meanders, raining) and buoyancy flux in other forms may form zonal jets called β-plumes where the Coriolis parameter varies with location geometrically or dynamically. The appearance of a simple β-plume is a westward stretching quasi-zonal circulation consisting of two jets flowing in opposite direction. This circulation originates from a continuous source of perturbation on the β-plane (or γ-plane) and develops via the emission of Rossby waves.

The β-plume concept was first introduced by Stommel (1982), when he described a two level beta-governing circulation driven by heat flux from the hydrothermal vents of the South Pacific Rise. In his model, the strong heat driven flows escape from the vents at the ridge and immediately entrain to a higher equilibrium level. It creates a two layer source-sink system (source at top, sink at bottom). As a result, two superimposed horizontal westward-propagating circulations are observed: anticyclonic in the upper layer due to the source; cyclonic in the lower layer due to the sink. Stommel suggests that these two circulations are dynamically active and spread westward under their own mechanism rather than as a passive tracer. He also suggest that the circulations would extend indefinitely westward in the absence of vertical diffusion.

Davey and Killworth (1989) further develop the β-plume mechanism through their model of a localized buoyancy forcing on a β-plane. Their results show: 1) when the source is weak, the β-plume is linear and the jet-like circulation stretches westward continuously at a long-Rossby wave speed; 2) when the source is strong, the β-plume looks like a chain of discrete eddies propagating westward; 3) the time scale for generating an eddy is proportional to that of a long Rossby wave propagating across the forcing region.

Three dynamical regimes of the β-plume circulations were summarized by Spall and Pickart (2003). The first is the forcing region, in which the balance is between vorticity input from the upwelling and advection across the mean vorticity gradient. The second dynamical regime is a zonal flow outside of the latitude range of the forcing and away from meridional boundary. Finally the circulation closes somewhere to the west in a viscous boundary layer in the third regime.

Many interesting examples of the β-plume in the ocean are provided. As described by Özgökmen et al (1999), the Azores current at about 35N, flowing eastward toward the Gulf of Cadiz is a β-plume. The denser Mediterranean overflow from strait of Gibraltar entraining lighter fresh water provides an effective sink for the clockwise β-plume. The eastward Azores current is actually the southern flank of the plume. This theory is then proved by the numerical study of Volkov and Fu (2010).

The theory presented here follows the theory from the paper by Afanasyev et al (2011). Considering a flow induced by a localized source on polar γ-plane where $f = f_0(1 - \gamma r^2)$ which will be discussed further in section (2.2). The total velocity of the flow is comprised by the geostrophic (subscript g) components and ageostrophic (subscript a) components,

$$\vec{V} = \vec{V_g} + \vec{V_a} \qquad (1.5)$$

with geostrophic velocity

$$\vec{V_g} = \frac{g}{f_0}\vec{k} \times \nabla\eta \qquad (1.6)$$

and ageostrophic velocity

$$\vec{V_a} = \frac{g}{{f_0}^2}\nabla\vec{\eta_t} - \vec{V_g}\gamma r^2 \qquad (1.7)$$

Here g is the gravitational acceleration, $f_0 = 2\Omega$ is the experimental Coriolis parameter for the rotating tank, η is the surface elevation and $\vec{k}$ is the vertical unit vector. The shallow water continuity equation can be used to introduce the mass flux per unit area by adding a source Q to the right-hand side of equation (Gill, 1982)

$$H_0\left(\frac{\partial u_a}{\partial x} + \frac{\partial v_a}{\partial y}\right) + \frac{D\eta}{Dt} = Q, \qquad (1.8)$$

where Q is represented the mass flux per unit area, H_0 is the water depth, ageostrophic terms are denoted by subscript a and geostrophic term is denoted by subscript g. The mass flux of our experiments is shown in Table (2). After substituting (1.6) into (1.7), linearize the advective term and transferom into polar coordinates (r, θ), we obtain

$$\nabla^2\eta_t - \frac{f_0^2}{gH_0}\eta_t - 2\gamma f_0\eta_\theta = -Q\frac{f_0^2}{gH_0}. \tag{1.9}$$

The solution of equation (1.9) can by written as

$$\eta = \sum_{m=-\infty}^{+\infty}\sum_{n=1}^{\infty}\eta^{mn}\, exp(im\theta)J_m\left(\alpha_{mn}\,\frac{r}{R}\right) \tag{1.10}$$

where α_{mn} is the n^{th} root of the Bessel function for the m^{th} order, R is the radius of the domain. Substituting the solution into (1.9), such that

$$\eta_t^{mn}\left(-\alpha_{mn}^2 - \frac{f_0^2}{gH_0}\right) + 2\gamma f_0 im\eta^{mn} = \frac{f_0^2}{gH}Q_{mn} \tag{1.11}$$

where Q_{mn} is the Fourier-Bessel transform for the source Q, such that (Arfken and Weber 2001)

$$Q_{mn} = \frac{1}{2\pi}\frac{2}{\mathrm{R}^2[J_{m+1}(\alpha_{mn})]^2}\int_0^{2\pi}d\theta\int_0^R Q(r,\theta)\, exp(-im\theta)J_m(\alpha_{mn}\frac{r}{R})rdr \tag{1.12}$$

Here the source Q can be presented as

$$Q = \sum_{m=-\infty}^{+\infty}\sum_{n=1}^{\infty}Q_{mn}\, exp(im\theta)J_m\left(\alpha_{mn}\,\frac{r}{R}\right) \tag{1.13}$$

After integrating the equation (1.11) with initial condition $\eta^{mn} = 0$ at t=0, we can obtain

$$\eta^{mn} = -\frac{4iQ_{mn}}{mf_0}(1 - exp^{i\omega_{mn}t}) \tag{1.14}$$

with dispersion relation

$$\omega_{mn} = \frac{2m\gamma f_0}{(\frac{\alpha_{mn}^2}{R^2} + \frac{f_0^2}{gH})} \tag{1.15}$$

The full solution of equation (1.9) is then obtained as

$$\eta = -i\frac{4}{f_0}\sum_{m=-\infty}^{+\infty}\sum_{n=1}^{\infty} Q_{mn}(1 - exp(i\omega_{mn}t))exp(im\theta)J_m\left(\alpha_{mn}\frac{r}{R}\right) \tag{1.16}$$

From the solution, we find that the wave transporting azimuthally westward.

This solution is similar as what Davey and Killworth (1989) obtained for the β-plume. If the term comes from dispersion ($\nabla^2\eta_t$) is ignored in equation (1.8), a long wave solution can be obtained, given in the form of the integral

$$\eta = \frac{4}{f_0}\int_{\theta}^{\theta+2\gamma f_0 \omega_{mn}{}^2 t} Q(r,\theta')d\theta' \tag{1.17}$$

Alternatively, an nondispersive wave solution that propagate purely to the west can be obtained by (1.15) with a simplified dispersion relation

$$\omega_{mn} = 2m\gamma f_0 R_d^2 \tag{1.18}$$

where $R_d^2 = (gH)^{0.5}/f_0$ is the barotropic radius of deformation. However, when the full dispersion relation (1.15) is used, the solution given by (1.16) is quite different. The wave transports much slower and has significant dispersion. The ratio of the terms in the denominator in (1.15) is

$$\frac{\alpha_{mn}^2 gH_0}{R^2 f_0^2} = \alpha_{mn}^2\frac{R_d^2}{R^2} \tag{1.19}$$

Chapter 2: Experimental and Analytical Method.

2.1 Introduction

All the experiments were performed at the Geophysical Fluid Dynamics (GFD) laboratory at Memorial University. The laboratory contains a rotating platform whose rotating rate is controlled by "WFC Ac Inverter" from the company TB Wood's. Experiments on rotating platforms are an important method in geo-physical (oceanic/atmospheric) fluid dynamics, especially where people pay attention to the planetary rotation. The experimental setups, and the Altimetric Imaging Velocimetry method will be described in this section.

2.2 Laboratory apparatus

A sketch of a typical experimental setup is shown in Fig. (4). All experiments were performed in a circular tank with diameter $D = 110$ cm filled with water to an average depth $H_w =$ 10 cm. The tank was installed on a rotating table and rotated counterclockwise at a rate of $\Omega = 2.5\ \mathrm{s}^{-1}$. The water in the tank was colored with black dye to eliminate the unwanted light reflection from the bottom. When the tank is rotating around the central vertical axis, the fluid surface becomes paraboloid, such that the depth of fluid changes with the radius as

$$h(r) = H_w + \frac{\Omega^2}{2g}\left(r^2 - \frac{R^2}{2}\right). \qquad (2.1)$$

Where $h(r)$ is the height of the free surface, H_w is the mean depth of the rotating fluid, Ω is the rotation rate of the tank, R is the radius of the tank, and g is the gravitational acceleration, and r is the radial distance from the axis of rotation on the horizontal plane. Since the depth of the rotating water is varying quadratically with the radius, the so-called β and γ-plane approximations can be applied as follows, which is useful for comparing our experimental analysis with those previously studied by other authors. Already well known, the potential vorticity (PV) can be defined as:

$$q = (f_0 + w)/h. \tag{2.2}$$

Where w is the relative vorticity, $f_0 = 2\Omega$ is the planetary vorticity and h is the total height of the fluid at any given point in the tank. When h with different radii is calculated, according to equation (2.1), we are allowed to write the potential vorticity as

$$q = \frac{f_0 + w}{h(r)} = \frac{f_0 + w}{(H_0)(1 + \frac{\Omega^2}{2gH_0} r^2)} \approx \frac{(f_0 + w)\left(1 - \frac{\Omega^2}{2gH_0} r^2\right)}{H_0}. \tag{2.3}$$

Where $H_0 = H_w - \frac{R^2\Omega^2}{4g}$ is the minimal depth of the fluid when the tank is rotating (usually at the center point of the tank). Assuming that the Rossby number

$R_0 = w/f_0 << 1$, potential vorticity can be rewritten as

$$q \approx \frac{w + f_0\left(1 - \frac{\Omega^2}{2gH_0} r^2\right)}{H_0}. \tag{2.4}$$

As a comparison, on a rotating sphere where f varies with latitude according to

$f = 2\Omega \sin\alpha$, the well known γ-plane approximation is described as

$$f = f_0[1 - \frac{1}{2}(\frac{r_s}{R_S})^2]. \tag{2.5}$$

Where r_s is the distance measured from the pole, $f_0 = 2\Omega$, R_S is the radius of the sphere, and $\gamma = f_0/2R_E^2$ is the gamma parameter of a rotating sphere. Using this approximation, the potential vorticity in the polar region on the rotating sphere has a similar form as the expression (2.4) for the rotating tank, where the Coriolis parameter also varies quadratically with the distance from center; such that

$$f = f_0 - \gamma r^2, \tag{2.6}$$

with $\gamma = \frac{\Omega^3}{gH_0} = 0.0031\, s^{-1}cm^{-2}$ for the laboratory system.

Next, we introduce a local β-plane approximation as $f = f_0 + \beta y$ where y is measured from intermediate radius. An approximate expression for the depth of the fluid in the vicinity of radius r_0 is given by $h(r) = h(r_0) - (\Omega^2 r_0/g)y$. Here, the y-axis of the local Cartesian system with the origin at r_0 is directed towards the pole. Then, the potential vorticity can be written as:

$$q \approx \frac{w + f_0\left(1 + \frac{\Omega^2 r_0}{\mathrm{gh}(r_0)} y\right)}{h(r_0)} = \frac{w + f_0 + \beta y}{h(r_0)} \tag{2.7}$$

Here, the dynamical equivalence between the rotating tank and the geometrically-varying Coriolis parameter on a rotating sphere is established by defining the β-parameter as $\beta = \frac{2\Omega^3 r_0}{g\mathrm{h}(r_0)}$. As shown in Fig. (3), the β-parameter is varied along a radius. The maximum value is $0.1153\, s^{-1}cm^{-1}$ when r = 40 cm.

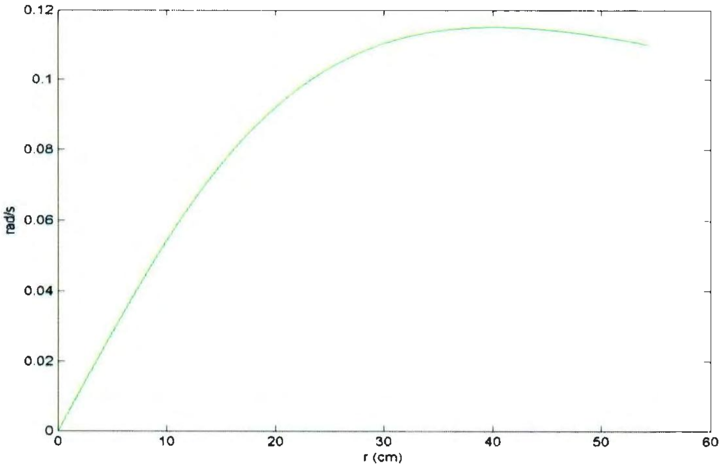

Fig.3 The profile of the β-parameter along a radius of the rotating tank. The β-parameter is varied along a radius.

In the fundamental experimental setup, a disk-shaped heater was used to generate an upwelling of warm water. The heater with radius $r_h = 7$ cm and with thickness $t_h = 1$ cm was fixed at the bottom of the tank at 16 cm from the wall (Fig. 4 (b)). Here the β-parameter is about 0.11 $s^{-1}cm^{-1}$ as shown is Fig. (3). When connected to a 120V AC power source, with the resistance $R_h = 15\ \Omega$, the power of the heater of is approximately 1000W. And the power supply was controlled by an Arduino board, which modifies the heater intensity by altering the switch-on time over two second intervals. For example, when the power supply is set at 25%, for every two seconds, the heater is on for the initial 0.5 s then off in the remaining 1.5 s, which makes the power of the heater equivalent to 240W. In a series of experiments, the frequency of the power supply was set to 10%, 25%, 45%, 65%, 80%, and 100%. In the second experimental setup, an eastward (counterclockwise) background flow was generated by a sink for the purpose of investigating the development of β-plume under background flows. In these series of experiments, two tubes connecting an electric pump were dipped into the water. The first tube (Fig. 4 (4)) with a distance 23 cm from the side wall was used to suck water and to generate the eastward background flow; the water was pumped out of the tank and then returned back to the tank through the second tube near the wall (Fig. 4 (4)). This setup not only maintains a constant volume of water in the tank but also creates an eastward flow originating from the first tube and stretched to the west (clockwise). The distance from the first tube to the wall was the same as the distance from the center of the heater to the wall (23cm). This setup located the heater in the center of the flow. In order to minimize the effect of the source on the circulation in the tank, the second tube was equipped with a diffuser (sponge) and located at the bottom of the tank.

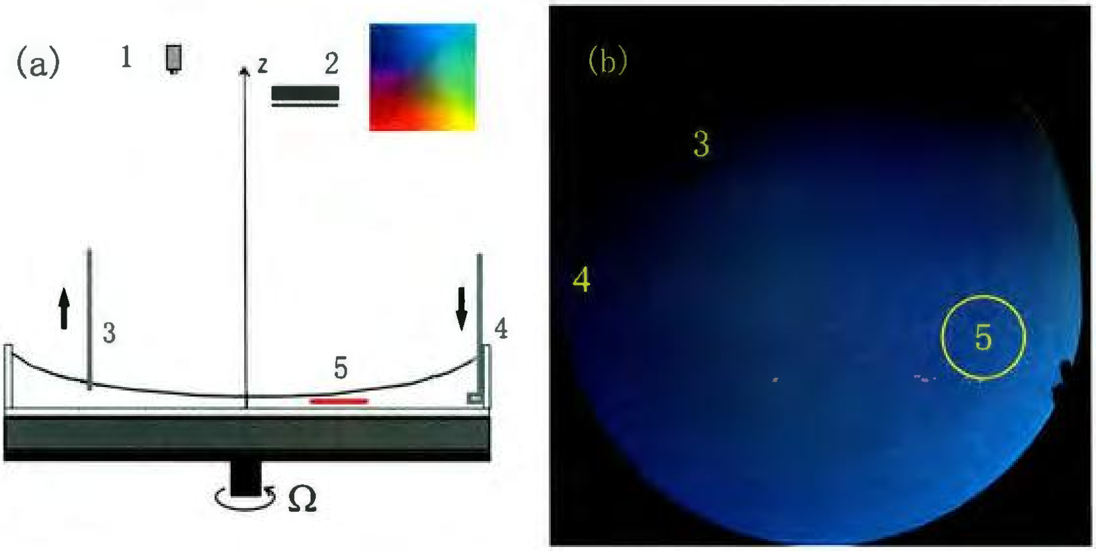

Fig.4 Sketch of the experimental setup (a) and a snapshot of the tank rotating at “null” speed when no flow is induced (b): digital camera (1), lamp box with color slide (2), tube (for sink) (3), tube (for source) (4), heat source (5), and the rotating tank (6).

In some experiments an infrared (IR) camera (Flir E30) with a 120 x 160 pixel array, was used to visualize and measure the surface temperature field in the vicinity of the heater. The baroclinic velocity can also be determined from the measured temperature field. The thermal wind equation allows us to relate the vertical shear of horizontal velocity with the horizontal gradient of density.

$$\frac{\partial \vec{U}}{\partial z} = -\frac{g}{\rho_0 f_0}(\vec{n} \times \nabla \rho) \qquad (2.8)$$

Approximately, the density is proportional to the perturbation temperature T, such that $\rho = \rho_0(1 - \alpha T)$. Here α is the thermal expansion coefficient and ρ_0 is the unperturbed density. Eq. (2.8) then takes the form

$$\frac{\partial \vec{U}}{\partial z} = \frac{g\alpha}{\rho_0 f_0}(\vec{n} \times \nabla T) \qquad (2.9)$$

2.3 Altimetric Imaging Velocimetry

The experimental data are analyzed by the Altimetric Imaging Velocimetry (AIV) method. AIV is an optical method to observe perturbations of a rotating fluid with a free fluid surface by measuring the slope of the surface elevation $\nabla\eta = (\frac{\partial\eta}{\partial x}, \frac{\partial\eta}{\partial y})$. The major dynamical fields such as geostrophic velocity, surface elevation and other variables can then be calculated from the surface slop field. The resolution of the results is very high which depends on the image resolution of the camera. By this method, we can easily get experimental analysis results such as quantitative separate images or animations of variables relative to the dynamical flow.

A brief sketch of the AIV setup is shown in Fig. 4 (Section 2.2). A tank filled with fluid on the rotating platform is essential for AIV method. When the tank is rotating around the central vertical axis, due to the balance between centripetal force and gravity, the free surface of the rotating fluid is a paraboloid described by (2.1) in the last section.

The system includes a high 5 megapix video camera capable of recording images at a rate of 10 frames per second and a high brightness monitor acting as a light source (Fig. 4 (1)). Above the water surface (in a rotating reference frame) the monitor (2) is located at height H but slightly off the rotation axis which is also the optical axis of the paraboloid. A color mask slide (Fig. 4 (a) insert) was displayed on the monitor. Each color on the slide is described by three parameters: lightness and chromaticities (*a* and *b*). The parameters *a* and *b* vary from negative to positive values with its position, as a result, the color changes from green to magenta in x direction and from blue to yellow in y direction on the slide. The reflection of the colorful slide on the monitor from the water surface is then observed by the camera.

When the tank begins rotating at a given rotation rate Ω, due to the changing curvature of the water surface, the reflection of the slide received by the camera gradually stretches over the entire water surface. The value of the null rotation rate Ω is determined by the geometry of the AIV setup. When the water is fully developed into a certain paraboloid corresponding to a certain rotating rate, the surface which is uniformly illuminated by nearly a single color, usually the color in the center of the light source (the slide) can be achieved. This field is named null field. When any flows are triggered on the present water surface (null field), the additive disturbances will change the surface slopes and the angles of the reflection as well. Consequently, a different point on the screen with a different color from null color (center of slide) will be reflected to the camera. So we can get multicolor images of the water surface with various flows.

The obtained multicolor images are then used to visualize surface slope $\nabla\eta$ which is the primary dynamic field. On each point of one image, a different color from the null field corresponds to a different location (*X*, *Y*) on the color screen from the slide's center point. Here the location *X* and *Y* are measured from the center of the screen. Then the two vectors which give the surface slopes at each point on the retrieved image can then be approximately obtained as

$$\left(\frac{\partial\eta}{\partial x},\frac{\partial\eta}{\partial y}\right)=\frac{1}{2r}(X,Y), \qquad (2.10)$$

where *r* is the radial distance from the rotating axis on the horizontal plane, η is the surface elevation. Further details of the method are described in Afanasyev et al. (2009).

Other fields can be calculated from the measured surface slopes by using the appropriate approximations. When the Rossby number R_0 is small (as in most of the rotating experiments, see Section 3.1), using geostrophic relationship as the first order approximation

$$f_0\vec{k}\times\vec{V_g}=-g\nabla\eta. \qquad (2.11)$$

Then the surface (barotropic) velocity field is given by equation

$$\vec{V_g} = \frac{g}{2\Omega_0}\left(-\frac{\partial\eta}{\partial y},\frac{\partial\eta}{\partial x}\right). \qquad (2.12)$$

Where $\vec{k}$ is the vertical unit vector. With the second order of approximation, total velocity of the flow can be written as a sum of geostrophic component $\vec{V_g}$ and ageostrophic component $\vec{V_a}$ as

$$\vec{V} = \vec{V_g} + \vec{V_a}. \qquad (2.13)$$

Where the ageostrophic component is given by equation,

$$\vec{V_a} = -\frac{g}{f_0^2}\frac{\partial\nabla\eta}{\partial t} - \frac{g^2}{f_0^3}J(\eta,\nabla\eta) + \gamma\frac{r^2 g}{f_0}(\vec{k}) \times \nabla\eta \qquad (2.14)$$

Here $J(A,B) = \frac{\partial A}{\partial x}\frac{\partial B}{\partial y} - \frac{\partial B}{\partial x}\frac{\partial A}{\partial y}$ is the Jacobian operator. This approximation for total velocity includes the geostrophic term, relatively small unsteady term, nonlinear term and γ term. One image is enough to calculate geostrophic flows at the first order; however, two consecutive images separated by a short time interval are required for the ageostrophic component. Two consecutive images of the flow separated by a short time interval are required to calculate the ageostrophic component. The calculated fields are more accurate when the dimensionless parameters Ro_T and Ro are small. In this thesis, AIV is used to solve the surface characteristic field of the fluid.

Chapter 3: Experiments Results and Analyses

3.1 Introduction

This chapter gives results from a series of experiments on flows generated by localized heating in the presence of a background zonal current on the polar β-plane. The related mechanisms include buoyancy flux, β-plume, and Rossby waves. In the series of preliminary experiments, we separately investigate the flows induced by a heater, and flows induced by a localized sink. The resulting flows without background jet will be discussed in sections 3.2-3.3. The characteristics of background zonal flows are controlled by the power of the electrical pump, which will be discussed in section 3.4. In section 3.5, the β-plume development in an eastward zonal background current is discussed. The main control parameters in the experiments are the strength of the heater, and the strength of the sink. The heater generates the β-plume, whereas the sink generates the background flow. This chapter is partially based on the paper by Afanasyev et al. (2009).

To better explain the GWS events on Saturn by the results of the laboratory experiments, some dimensionless parameters are investigated for dimensional analysis.

The Rossby number, R_0

The Rossby number $R_0 = U/fL$ shows the ratio of inertial force to Coriolis force, and also measures the influence of background rotation on fluid motion. Usually, in oceanography, rotation effects become important when the Rossby number is on the order of unity or less. For the GWS events on Saturn, the Rossby number is approximately 0.018. Here, we take a typical value for the dimensional horizontal velocity U = 0.03 km/s, a length scale of the storm head L = 8000 km

(Sa´nchez-Lavega, 2011), and the Coriolis parameter $f = 2\Omega_s \sin 37° = 2 \times 10^{-4} s^{-1}$ at 37°N where the storm head located. As for comparison, the Rossby number of the laboratory experiments is approximately 0.0143. Here, we take a horizontal velocity scale $U = 0.5$ cm/s and a characteristic scale of the flows $L = 7$ cm in the experiments. And the characteristic scale of the flows is the radius of the heater. The Rossby number of the laboratory experiments is similar to that of the GWS event. The two close Rossby numbers indicate the dynamical similarity between the laboratory experiment and the GWS event on Saturn.

The Ekman number, E_k

Another important dimensionless parameter that can characterize the importance of friction relative to Coriolis force is the Ekman number $E_k = 2\mu / f L^2$. Here, μ is the kinematic viscosity of the fluid. We take $\mu = 1 \times 10^{-6} \mathrm{m}^2/\mathrm{s}$ which is the kinematic viscosity of the water (20°C), and get that $E_k = 8 \times 10^{-6}$ for our experiment. The Ekman number for the atmosphere of Saturn may be very small (approximately 2×10^{-12}) when taking the kinematic viscosity $\mu_s = 0.01\ \mathrm{m}^2/\mathrm{s}$ (Tiscareno et al., 2007).

Baroclinic Instability & Rossby radius of deformation, R_d

In a baroclinic flow, the potential density does not only depend on pressure, but also on potential temperature such that $\rho = \rho(p, T)$. Baroclinic instability, also referred to as shear instability, is a process by which perturbations draw energy from the mean flow potential energy (R. Grotjahn, 2002). In our experiments, after the heater was on, the turbulent region that above the heater is filled with cyclone and anticyclone eddies (see section 3.2). That turbulent region is clearly baroclinic due to the vertical shear of horizontal temperature gradient created by upwelling warm water.

The region will expand and propagate to the west. Here, baroclinic instability have the tendency to decrease the vertical shear and provides the kinetic energy to sustain the eddies.

Rossby radius of deformation is an inherent horizontal scale that waves or particles travel before being significantly affected by the background rotation. The baroclinic radius of deformation can be defined as

$$R_d = \sqrt{\frac{g\Delta\rho H_0}{\rho_0}}\frac{1}{f_0}, \tag{3.1}$$

where g is the acceleration due to gravity, $\Delta\rho$ is the density difference between the warm water from heater and the ambient water in the tank, H_0 is the average water depth in the rotating tank, ρ_0 is the density of the ambient water in the tank, and $f_0 = 2\Omega$ is the Coriolis parameter. Here Ω is the rotation rate of the tank. In some supplemental experiments, the water temperature was measured by an IR camera. The intensity of the heater in these experiments is 100%, which is the same intensity of the heater in Exp. A1. The temperature of the ambient water was measured to be 20.2°C (Fig. 5 (a)). We can clearly see that the warm water was continually rising with time until it reached 40°C. The temperature does not distribute uniformly which means that the baroclinic radius of deformation was continually changing and took a non-uniform distribution. The baroclinic radius of deformation was calculated by the temperature measured at the center spots (See Table (1)). The average baroclinic radius of deformation is 1.2 cm (see Table (1)) which is calculated by the temperature measured at the center spots (Fig. 5). Note that baroclinic radius is typically equal to the scale of the eddies. Therefore, the gradually increasing scale of the eddies can be explained by the increasing of baroclinic radius of deformation. The increasing scale of the eddies in each of experiments is shown in Table (6).

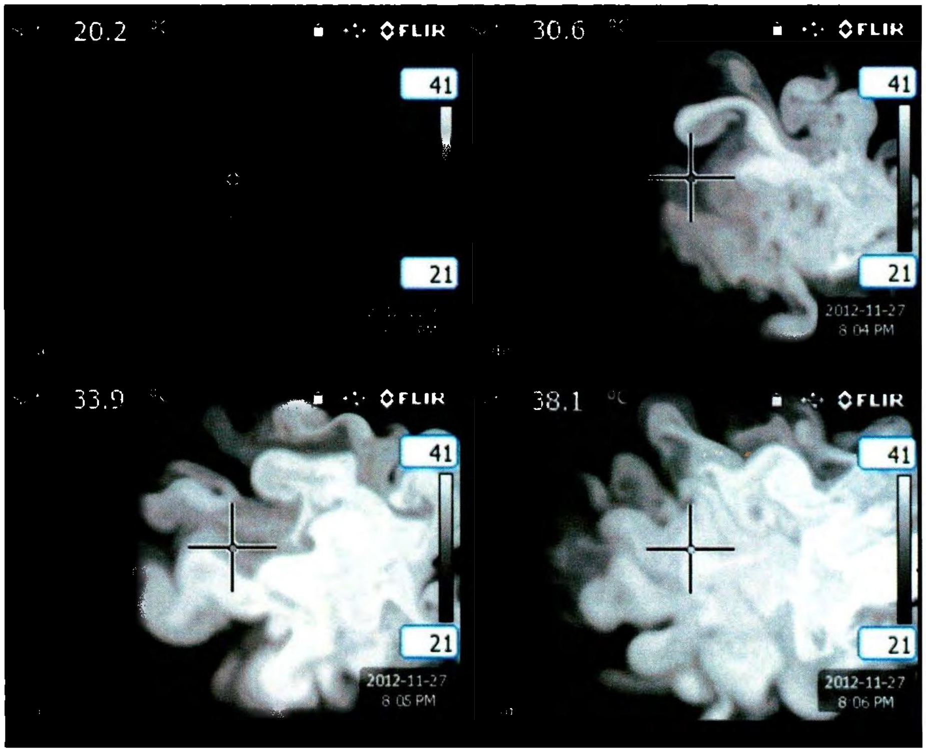

Fig.5 The images show temperature distribution of a developing beta-plume. The images are taken by an IR camera in a supplemental experiment. They are taken at different time: 48s (a), 151s (b), 203s (c), and 276s (d).

Barotropic Instability & Rayleigh-Kuo inflection criterion

In a barotropic flow, the fluid density only depends on the distribution of pressure. That means isopycnal surface, isothermal surface, and isobaric surface are parallel to each other. Compared to baroclinic instability, barotropic draws energy from the horizontal shear (R. Grotjahn 2002). In our experiment, as described in A. G. Slavin (2012), the barotropic region is located westward of the turbulent region which locates above the heater.

When warmer and lighter water is upwelled and interacting with the ambient water, the baroclinic instability is clearly present in the flow due to the vertical shear. However, it is also interesting to investigate as to whether the barotropic instability is involved as well. For that purpose, we apply the Rayleigh-Kuo inflection criterion.

The criterion gives a necessary condition for barotropic instability: the gradient of the total absolute vorticity will change sign within the domain. As shown in Fig. (6), the black line shows the profile of the azimuthal velocity U crossing the heater. The red line shows that the value of the expression $\beta - U_{rr}$ changes the sign along the plume. Here U_{rr} is the second derivative of the azimuthal velocity along the radius. Fig. (6) tells that the flow is potentially unstable due to the barotropic instability.

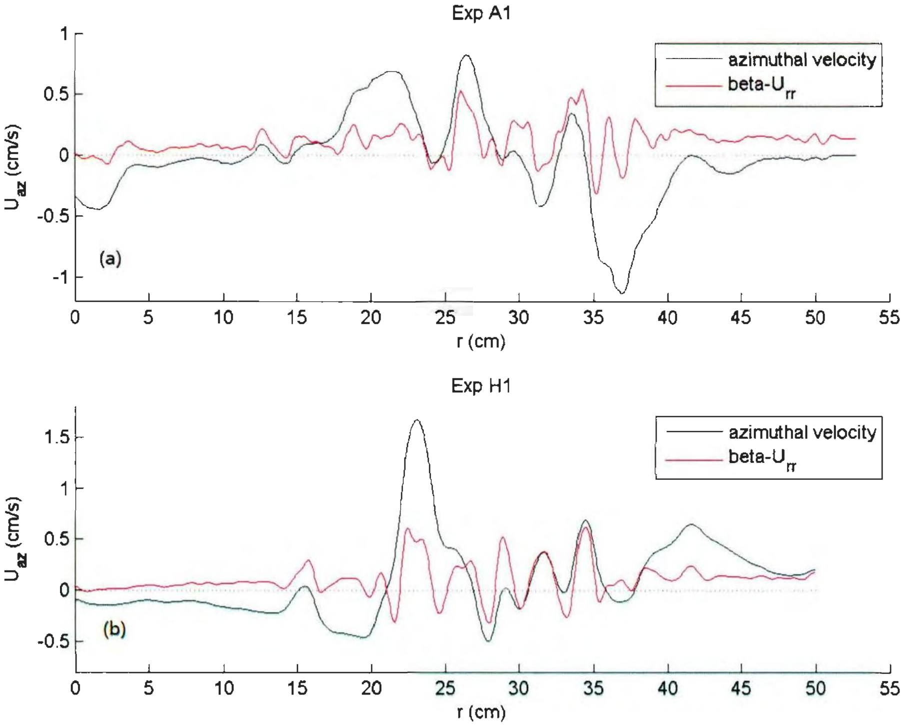

Fig.6 The black lines show the profile of azimuthal velocity U along the line 1 (a radius of the tank which also locates on the westward of the region above the heater) in Fig. 17 (a); The red lines are the values of the expression $\beta - U_{rr}$. (a) is measured from exp. A1 without the background flow (at 120 s) and Fig. (b) is measured from Exp. H1 with a strong eastward background flow (at 120 s).

Note that the effective beta ($\beta'(y) = \frac{\partial \overline{q}}{\partial y} = \beta(y) - \frac{\partial^2 \overline{u}}{\partial y^2}$) (Aguiar et al. 2010) on Saturn was also negative from 38°N to 43°N where the strong zonal winds exist (Fig. 9 c).

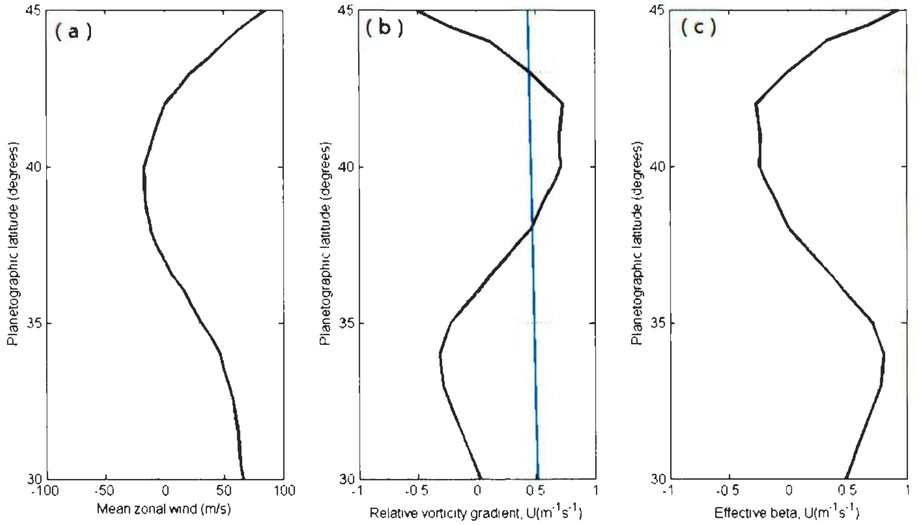

Fig.7 Mean zonal winds on Saturn (a), associated gradient of vorticity (black line) and planetary vorticity β (blue line) (b), and effective beta (c)

3.2 Turbulent Convection

In order to study the flow generated by the heater only, the first series of experiments (A1-6 in Table 3) was performed without any background zonal flow. In our experiments, buoyancy forcing was provided by a heat source fixed at the bottom of the rotating tank. After turning on the heat source, an upwelling flow was generated, which was analogous to the initial procedure of the generation of GWS. Laboratory turbulent convection created by a buoyancy source on the *f*-plane was studied in detail by Fernando et al. (1991) and Maxworthy and Narimusa (1994) (the process of flow generation is shown in Fig. 8). After the buoyancy flux was started, an upward propagating turbulent layer formed immediately. The theoretical time involved in this process is less than $1/f$, which is 0.2s in our experiment. Here, *f* is the Coriolis parameter. The movement of the water parcel within this turbulent mixed layer was a three dimensional disorder and almost unaffected by the background rotation of the fluid. The thickness of this immediately formed turbulent layer was approximately $Z_t \approx 1.2(B_0/f)^{1/2}$, as also found by Fernando et al (1991) and Hunt (1984). Here, B_0 is buoyancy flux per unit area. B_0 and thickness Z_t of each experiment are calculated and given in Table (2).

As shown in Fig. 8 (b), the thickness of the turbulent layer grows with time and finally reaches a transition thickness $\mathrm{Z_m}$. Above this transition level, background rotation becomes dominant instead of molecular effect. Many upward penetrating cyclonic vortices would be generated from this thickness. Rossby number at this transition thickness is $Ro_f = 2B_0^{1/3}/Z_m^{2/3}f = 0.37$ (Maxworthy, 1994). Using approach of Fernando et al. (1991) and Maxworthy (1994), the average transition depth can be calculated as:

$$Z_m \approx 13(B_0^{1/2}/f^{3/2}). \qquad (3.2)$$

In our experiments, the transition thickness is considered to be small, $Z_m = 0.37 - 0.73\ cm$ (See Table 2). Thus, the layer above the heat source is mainly occupied by rotation-dominated convection.

As shown in Fig. 8 (c), these vortices eventually propagate to the surface and form rotating water columns. Thereafter, the water columns 'full filled' the space above the heat source and 'tilt' took a conical shape. Due to the 'tilt', the water columns became unstable and established a baroclinic instability condition. At a later time, the upward penetrating water columns as convective vortices were made up to be several larger baroclinic vortices propagating away above the heater. According to Maxworthy and Narimousa (1994), the upward-propagating speed of the quasi-2D vortices in the form as:

$$W_v = (B_0/f)^{1/2} = 0.15 - 0.28 \text{ cm/s}. \qquad (3.3)$$

Note that the vertical velocity of the upwelling wind of the GWS is about $100\ m/s$ (Sanchez-Lavega, 2011). Assume that the function (3.3) can be applied to the great storm on Saturn, than the buoyancy flux of its source/material was calculated as $B_0 = W_v^2 f_s = 1\ m^2/s^3$.

In our experiments, the average diameter D_v of the baroclinic vortices generated by buoyancy flux in the initial period can be estimated by Maxworthy and Narimousa (1994) as:

$$D_v = 15(B_0^{1/2}/f^{3/2}\ ) = 0.42 - 0.85\ cm. \qquad (3.4)$$

In order to check the consistency of our results with this estimation, the diameter of the baroclinic vortices was measured. We measured the velocity profiles along the diameter of the eddies in the Exp. A1-A5 (See Table 3). The profiles show the scale of the eddies in our experiments. The profiles of three eddies in Exp. A1 (Fig. 9) show that the average diameter of these three eddies is 3.1 cm. The value continually decreases from Exp. A1 to A5 due to the decreasing of the intensity heat source in these experiments. This is reasonable when considering the buoyancy flux is proportional to the intensity of the heater. The average eddy diameters of Exp. A1-A5 was measured as $0.8 - 4.2$ cm (see Table (6)), which is larger than theoretical prediction (equation 3.4).

In common situations, we can also consider a source of buoyancy flux to be a source of mass flux. The mass flux above the heat source with different power can be estimated as the product of the upwelling velocity and the area of the heat source,

$$Q_m = W_v * A_0 = 21 - 43\ cm^3/s. \qquad (3.5)$$

Here $A_0 = 153.86\ \text{cm}^2$ is the area of the heater. The results of Q_m in each experiment are shown in Table (2).

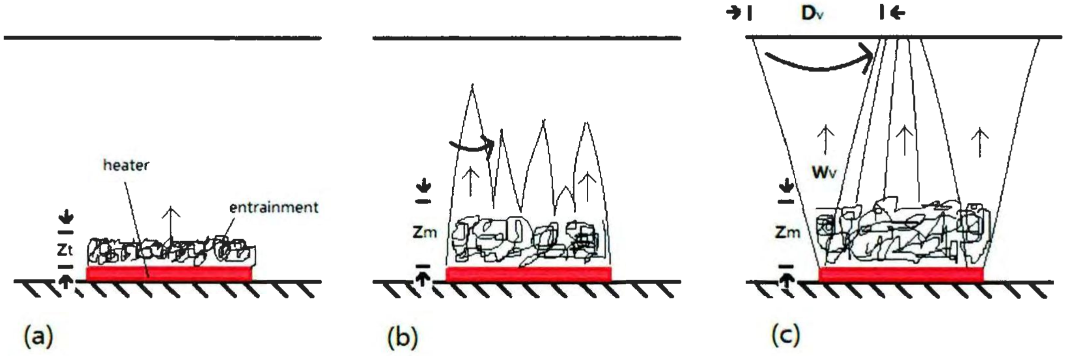

Fig.8 Schematic of the sequence of events that occurs after a buoyancy flux is triggered at the bottom of a rotating tank. (a) A turbulent layer is immediately formed after the heater is activated. The flows in this layer are disorderly; (b) after the thickness of the turbulent layer reaches a transition level, rotational effects became important. Many cyclone vortices are generated; (c) the vortices reach the water surface and establish a baroclinic instability.

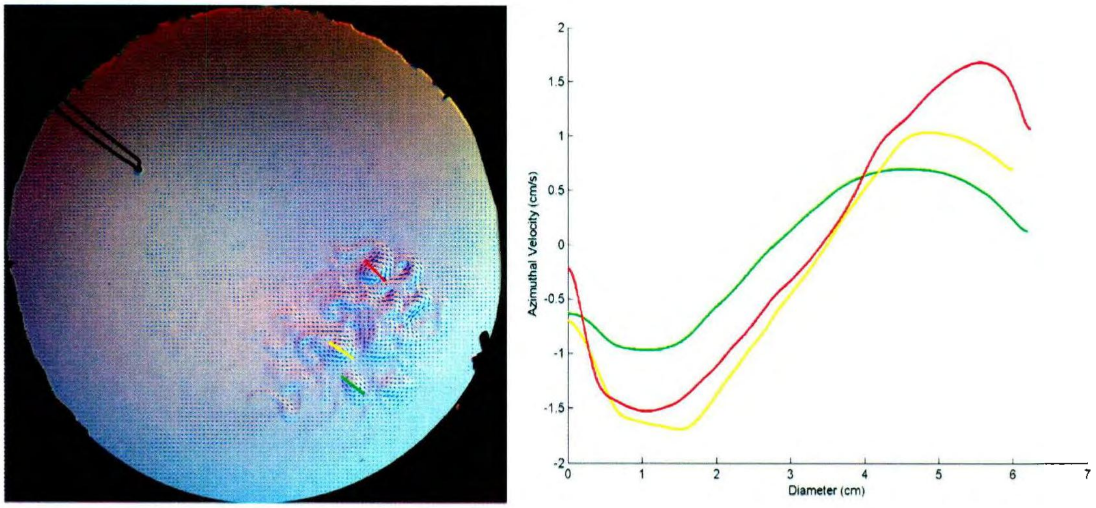

Fig.9 The left image shows the geostrophic velocity in Exp. A1 at 180s. The right image shows the velocity profiles along the diameters (straight lines in the right graph) of the three vortices. It gives an average diameter of these three vortices to be 3.1 cm.

The real observation of the convective flow is shown in Fig. 10. When the system was in solid-body rotation, the heater was activated to generate warm water. The warm water is lighter than the ambient water, so it rose to a higher region above the heater. Observations show that warm water from the heater rises to the surface and creates a turbulent flow with multiple eddies. Fig.10 shows a magnified picture of the surface area above the heater shortly after turning on the heater (t = 28s). The surface barotropic velocity field Fig. 10 (a) reveals an intense jet-like flow at the periphery of the area above the heater. This is a typical frontal jet which flows clockwise. Some other frontal jets flows anticlockwise (cyclones) can also be observed around the central part of the area. It seems that these circular cyclones are associated with the local downwelling of relatively cool water from the surface, where convergence of horizontal velocity results in cyclonic circulation. As expected, the associated vorticity map in Fig. 10 (c) shows both cyclones (red) and anticyclones (blue). It is interesting to note that the anticyclones are mainly in the form of elongated bands, while cyclones are often of circular form. Fig. 10 (b) shows a surface temperature map measured by the IR camera together with the baroclinic velocity field. The vertical shear of baroclinic velocity was calculated by Eq. (2.9). The shear was then multiplied by h/2, the half-depth of the fluid, to obtain an estimate of velocity. The effective thickness of the warm lens for estimation will be discussed later (Eq. 3.4) in this section.

A comparison of plates Fig. (10 a) and Fig. (10 b) shows that the direction and magnitude of the barotropic (AIV) and baroclinic (IR) velocities are generally similar. The differences between them can be revealed by comparing the corresponding vorticity fields in Fig. (10 c) and Fig. (10 d). The baroclinic vorticity field consists mainly of narrow bands of paired positive and negative vorticity which correspond to intense frontal jets. However, the barotropic vorticity is much less concentrated.

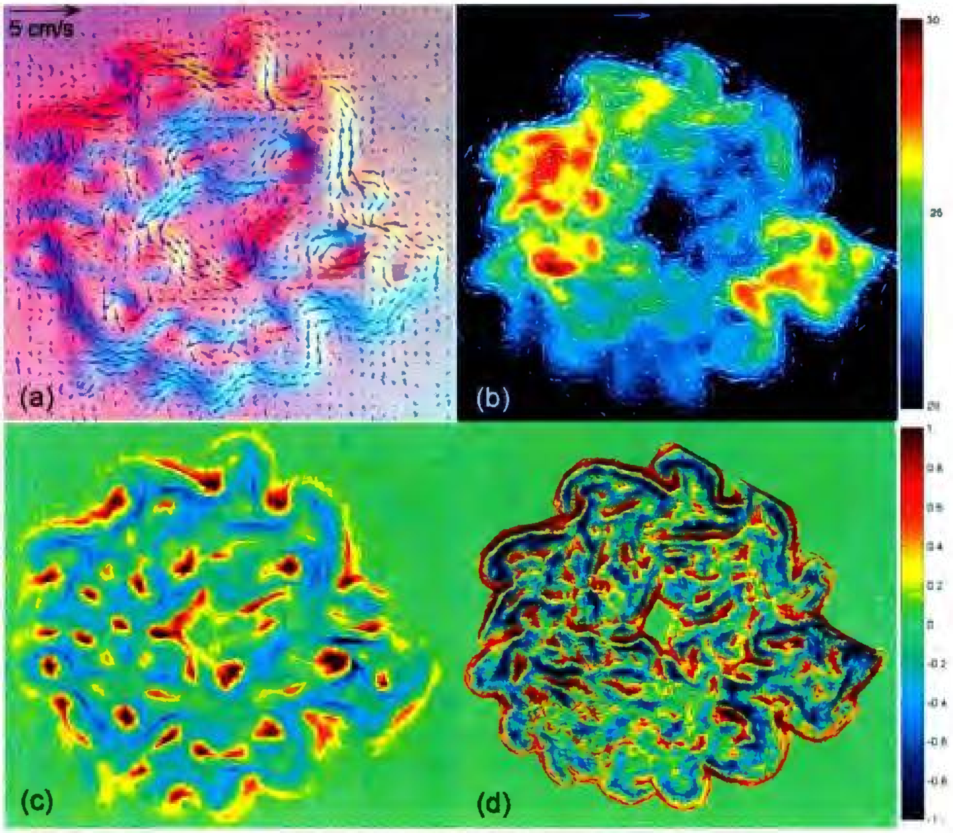

Fig.10 Flow above the heater (at 28 s) after turning on the heater in the experiment A1 (Table 3). (a) Barotropic velocity vectors superposed on the altimetric image of the flow. (b) Baroclinic velocity vectors superposed on the temperature field measured by IR camera, color scale shows temperature in °C (c, d) Relative vorticity fields calculated using the barotropic or baroclinic velocity respectively. The color scale shows dimensionless vorticity ξ/f_0 in the range from –1 (blue, anticyclonic) to 1 (red, cyclonic).

In this initial process, what drives the rising entrainment is the buoyancy flux generated by the heater. The radius r_1 of the expanding lens of warm water was measured for different intensities of the heater (Fig. 11). It is measured from the center of the heater to the east edge of the lens (as the black line in Fig. 12 (a)). This measuring method was designed for avoiding the influences on the lens of β-plumes which propagate westward from the heater. The measurements show that the area of the lens increases initially at an approximately constant rate before being stable at some constant value. After the area of the lens expanded to be a constant value, the expanding stops and the area stayed the same. The constant value of the area of the lens is different from Exp. A1-5. Heating with higher intensity has a larger constant value of the area of the lens. The warm water transported to the west due to the β-plume may be one reason to explain why the expansion stops. The expanding rate of the lens varies linearly with the upward propagating speed of the warm water (see Table 5 and Fig. 11(b)). The linearly fit in Fig. 11 (b) shows

$$dA/dt = 1.9A_0W_v/h. \tag{3.6}$$

Here, $A = \pi r_1^2$ is the area of the lens, $A_0 = 153.86\ \mathrm{cm}^2$ is the area of the heater, and h is the mean water depth in the tank. Assuming that when the warm water is rising from the heater to the surface and spreads in a horizontal direction, a layer with thickness h_1 was formed. If taking the upward volume flux of the water from the heater is equal to the horizontal expanding rate (divergence) of the upper layer, we obtain that

$$W_vA_0 = h_1dA/dt. \tag{3.7}$$

Substituting (3.2) into (3.3), we can get that $h_1 = 0.53h$. Thus the thickness of the expanding upper layer is approximately one half of the total depth h. When considering the upper layer of warm water as an inverse gravity current, the result is reasonable when compared to the studies of the exchange gravity flows. As shown in the studies by T. Brooke Benjamin (1967) and J. O. Shin et al. (2004), when the flow of the gravity current is steady and free from energy dissipation, the receding stream must occupy half the space originally occupied by the lighter (heavier) fluid.

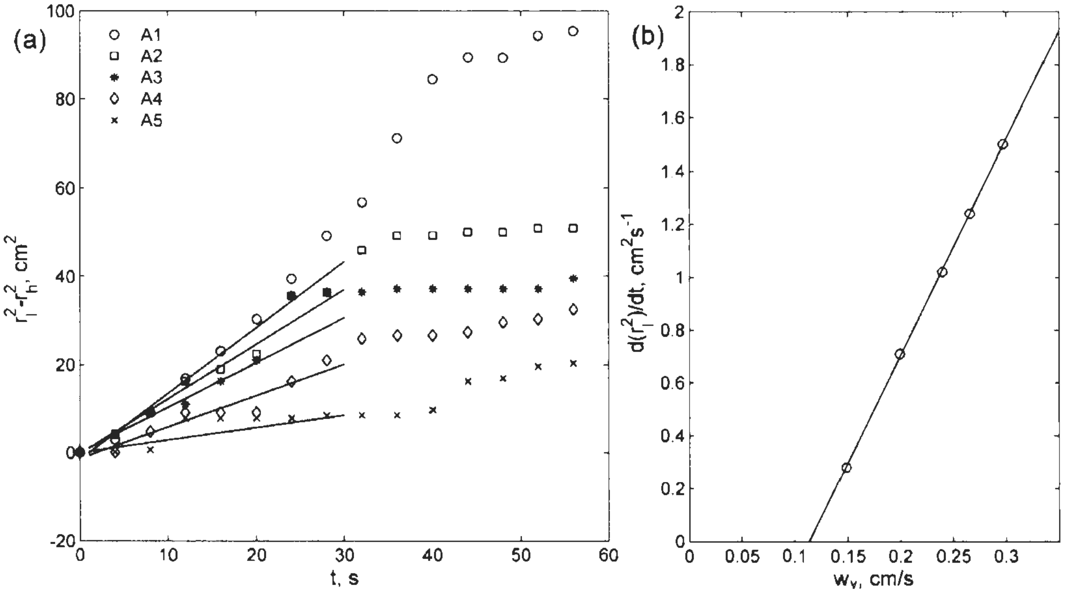

Fig.11 Expansion of the area of the warm water lens above the heater in experiments A1-5. (a) $r_1 - r_h$ as a function of time. Solid lines show a linear fit to the data during the initial period. (b) Rate of change of the area in the initial period of flow evolution versus the upwelling velocity W_v. The solid line shows a linear fit.

3.3 Simple β-plumes Model

In this section, we modeled a simple β-plume by upwelling water (as Fig. 12). The upwelling warm water was created by a heat source (disk-shape heater) fixed at the bottom of the rotating tank (16 cm from the wall). A few seconds after turning on the heater, turbulence occurred above the heater and expanded slowly. The expansion would stop when the warm water lens reach a certain radius. Meanwhile, zonally-elongated barotropic Rossby waves are emitted westward (clockwise) from the region above the heater, such that several westward traveling β-plumes generated from the turbulence area could be clearly observed. Here, warm water which rose above the heater and formed clockwise and anticlockwise eddies changed the water density and generated a baroclinic state. Then the baroclinic region emitted Rossby waves and expanded to the west. The observations of zonally elongated waves/jets are consistent with the previous experimental and numerical results of Afanasyev et al. (2011) and Slavin and Afanasyev (2012). Fig. 12 (b) shows the relatively high surface is carried by Rossby waves of relatively short wavelength in zonal direction from the area above the heater to the west.

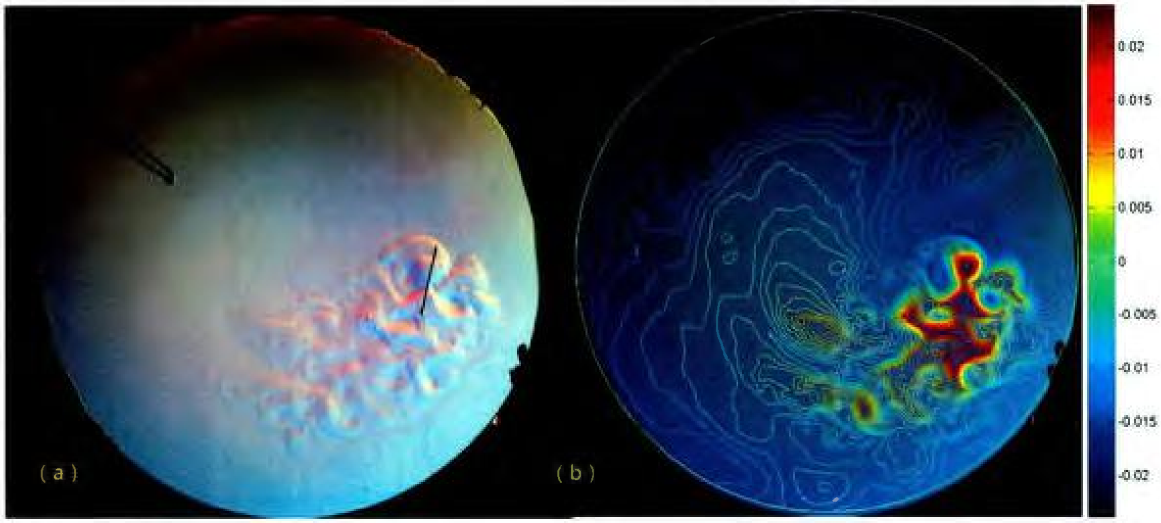

Fig.12: The image taken from experiment A1 at 320s shows the development of the β-plumes (a). The black line shows water expansion radius. The associated surface elevation by AIV is shown in (b).

Fig. 13 (a-d) shows snapshots of the flow with clear β-plumes. They are separately measured at of Exp. A4 (t= 140s, 320s) and Exp. A4 (t= 140s, 320s)). Their barotropic azimuthal velocity (color inserts) which are visualized by the AIV method, indicates the direction of jets associated with the plumes. The color of the inserts tell the azimuthal velocity of the surface water varying from -1 cm/s (blue) to 1 cm/s (red); red and yellow indicate eastward (anticlockwise) velocity, whereas blue and green indicate westward (clockwise) velocity. It shows some zonal flows with opposite direction alternate with each other along the radial direction. The flows inside each β-plume form a clockwise circulation that can be observed from inserts. Thus, long Rossby waves of almost zero-frequency establish a stationary circulation in β-plumes. Each β-plume is a gyre consisting of two jets flowing in opposite directions. The azimuthal directions of those circulations in Fig. 13 (b, d) are shown by arrows.

Fig. (13) also shows that the propagating velocity of the front of the β-plume has a positive relationship with the intensity of the heater. The intensity of heater supply was controlled by an Arduino board by altering the switch-on time within two second intervals. By comparing the position of the front of the plumes in Fig. 13 (a, b) and in (c, d), the transporting speed of β-plumes driven by a heater with high intensity (100 %) was clearly faster than that with low intensity (45%).

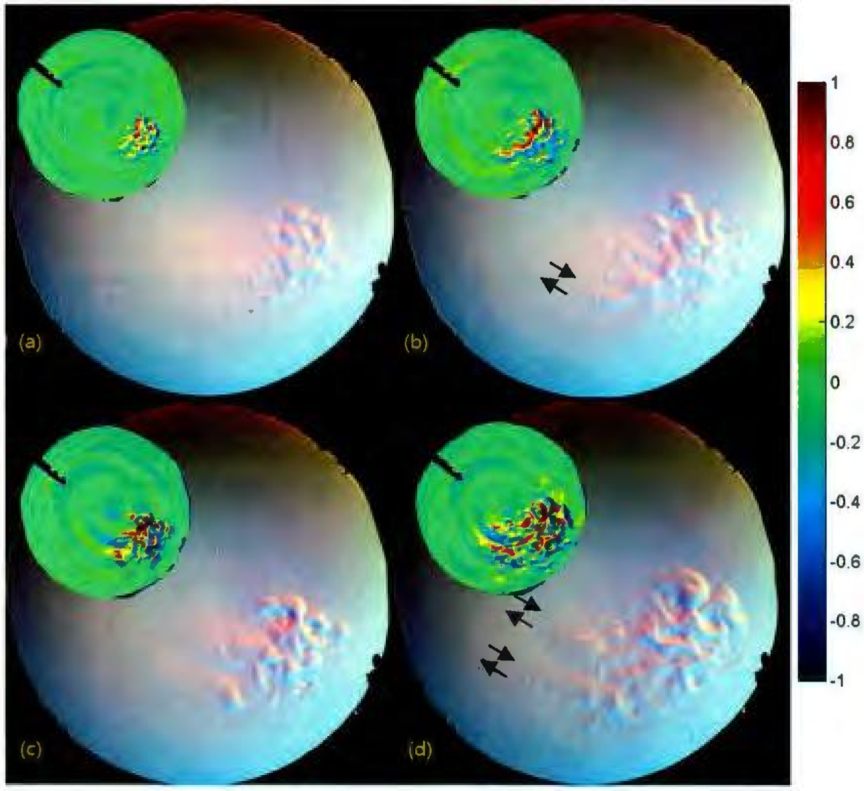

Fig.13 Development of β-plumes in Experiment A4 (100 %) measured at t = 140 s (a), 320s (b), and Experiment A1 (45 %) measured at t = 140s (c), 320 s (d). The inserts show the color maps of azimuthal velocity varying from -1 (blue) to 1 cm/s (red)

The relationship between the jets in β-plumes and the intensity of the source was investigated. The averaged velocity profiles (Fig. 14) along a radius tangent to the west edge of the heater (red line shown in Fig. 17 (a)) were measured. The data is averaged over 21 measurements taken from 320s to 400s with a 4s sampling interval, when β-plumes were well formed. The westward velocity along the southern flanks of the β-plume dominates a radial range from 25-30 cm to 37-42 cm. The eastward velocity along the northern flanks dominates the radial range from 20-25 cm to 32-37 cm. In Exp. A5, westward velocity and eastward velocity are also observed around the region of heater. Both the flows driven by stronger heater intensity (100%) are clearly faster than those under lower heater intensity (25%). It means the peak velocity of the circulation in β-plumes has a positive relation to the intensity of the buoyancy source, and that will be proven by the formulation (3.11). The calculation of the buoyancy flux and the peak velocities of the zonal flows and the eastward flows are shown in Table (3) and Fig. 16. They show both components of velocity in the β-plume are proportional to the vertical velocity W_v (or the intensity of the buoyancy source) in the turbulent area.

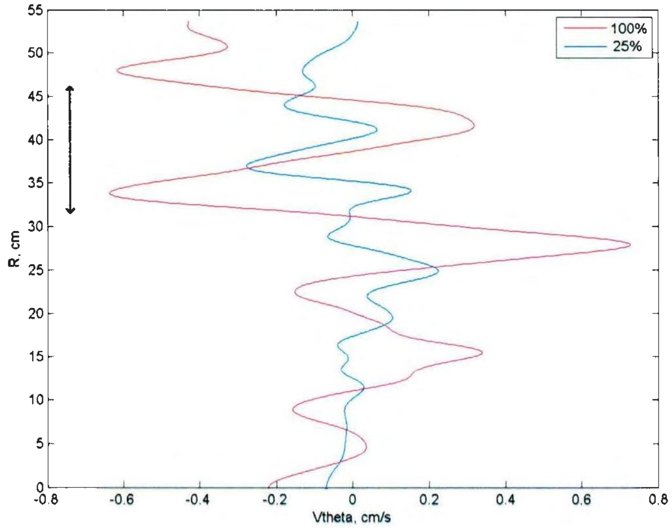

Fig.14 Time averaged azimuthal velocity profiles measured west of the source (red line shown in Fig. 17 (a)). The blue line shows the time averaged data for Experiment A5 (25% intensity) from 320s to 400s. The red line shows the time averaged data for Experiment A1 (100% intensity) from 320s to 400s. The double arrow indicates the radial extent of the heater.

All peak values of the westward velocity U_{west} in the time-averaged (from 320s to 400s with a 4s sampling interval) azimuthal velocity profiles for experiment A1-A6 are plotted in Fig. (15) *versus* the vertical velocity W_v from the buoyancy flux B_0 (See Table 2). The linear fit gives us

$$U_{west} = 2.1W_v. \qquad (3.8)$$

Here we try to compare the laboratory result to the theory (1.17). Substituting (3.5) into (1.17), the solution shows that the elevation of the surface η due to upwelling is uniformly extended westward from the perturbation area such that

$$\eta(r,\theta) = \frac{4}{f_0}\int_{\theta}^{\theta+2\gamma f_0 {\omega_{mn}}^2 t} W_v(r,\theta')d\theta'. \qquad (3.9)$$

Where (r,θ) is the polar coordinate system with the origin at the center of the tank, and the upper integration limit $\theta + 2\gamma f_0\lambda^2 t$ is the eastern boundary of the perturbation area. Thus, the surface elevation is in the form of a "ridge" stretching along the zonal direction. Due to the geostrophic flow relationship, two jets will flow in opposite direction on the northern and the southern slopes of the ridge with velocity given by

$$\vec{U} = \frac{g}{f_0}(\vec{n}\times\nabla\eta) = \frac{g}{f_0}\left(-\frac{1}{r}\frac{\partial\eta}{\partial\theta},\frac{\partial\eta}{\partial r}\right). \qquad (3.10)$$

Substituting (3.9) into (3.10), the radial velocity is given by

$$U_r = -\frac{4g}{rf_0^2}W_v. \qquad (3.11)$$

It means the radial component of velocity exists only within the area of the perturbation (area of W_v), and the radial transport is the same as the zonal transport in each of the jets, connecting the zonal jets. Similarly, the azimuthal velocity is given by

$$U_\theta = \frac{4g}{f_0^2}\frac{\partial}{\partial r}\int_{\theta}^{\theta+2\gamma f_0\lambda^2 t} W_v(r,\theta')d\theta'. \tag{3.12}$$

Note that the factor $4g/rf_0^2$ is equal to 4.5, which is reasonable when comparing with the experimental result 2.1 in (3.8), where the exact distribution of the W_v across the area above the heater is unknown.

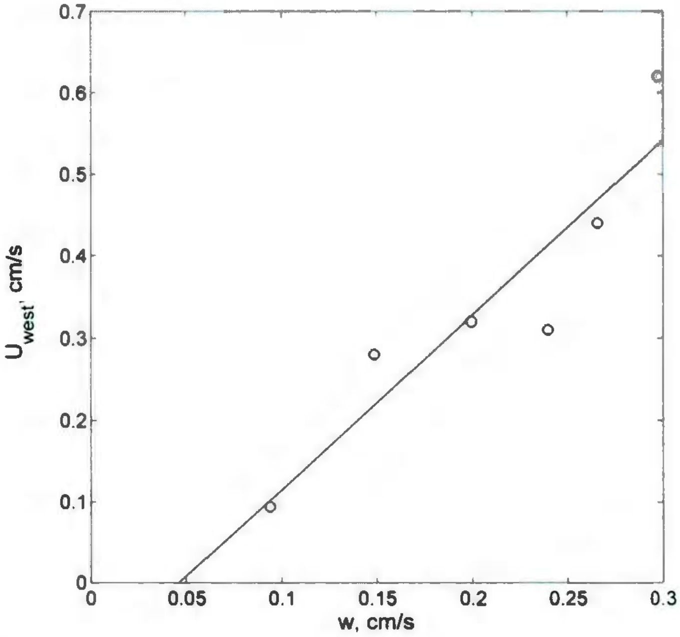

Fig.15 Peak westward velocity U_{west} from time averaged data (from 320 s to 400 s) of Experiments A1-6 versus the upwelling velocity W_v in the same experiment. The solid line is a linear fit of slope 2.1.

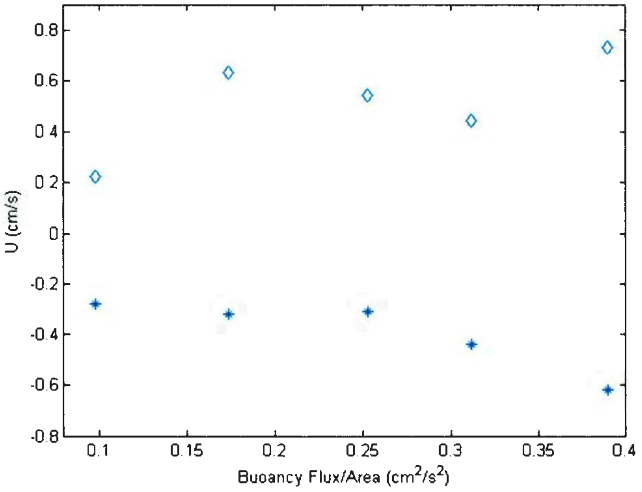

Fig.16 Peak velocity (eastward and westward) of time averaged azimuthal velocity profiles measured at 20° west of the source (red line shown in Fig. 17 a) with buoyancy flux. The diamonds and the stars show the eastward and westward peak velocity, respectively

3.4 Background Zonal Flow

In the second series of experiments (B-H), the effects of the background flow on a β-plume were investigated. For this purpose, a background eastward (anticlockwise) flow was introduced by a sink (10 o'clock in Fig. 4). The intensity of the sink was controlled by regulating the voltage of the pump (see Table 3). After switching on the pump, a clear band of eastward flow originates from the sink and extends to the west (clockwise) (Fig. 17). The eastward flow starts at the latitude of the sink and extends southward almost to the boundary of the tank. At the same time, a westward flow extends northward from the sink. The flows are due to a β-plume generated by the sink. However, this β-plume has an opposite circulation to the one generated by the heater in the last section; that is, it has an eastward flow at the northern flank and a westward flow at the southern flank. It is reasonable when considering the sink acted as a negative source of buoyancy flux. In some experiments, some transient phenomenon such as small (barotropic) cyclonic vortices separating from the sink can be observed. However, they would decay to be negligible before reaching the longitude of the heater. Note that the actual picture of the circulation in the tank is somewhat different from that of a single β-plume due to the sink. This may be explained by the diffused source located at the wall at approximately 9 o'clock (see Fig. 4).

All measurements and experiments were taken after starting the sink, and enough time was given to allow a stationary circulation to form. To investigate the features of the background flow, azimuthal velocity profiles along 3 lines (20° west, center and 20° east of the heater, see Fig. 17 (a)) were measured for each experiment. As the example shows here, both the width and the peak velocity of the plumes caused by the stronger sink are larger than that of a weaker sink. This means the background flow speed has a positive relationship with the sink's intensity. Note that the radial position of the sink was chosen such that the heater was located at the center of the eastward jet (R = 35 cm).

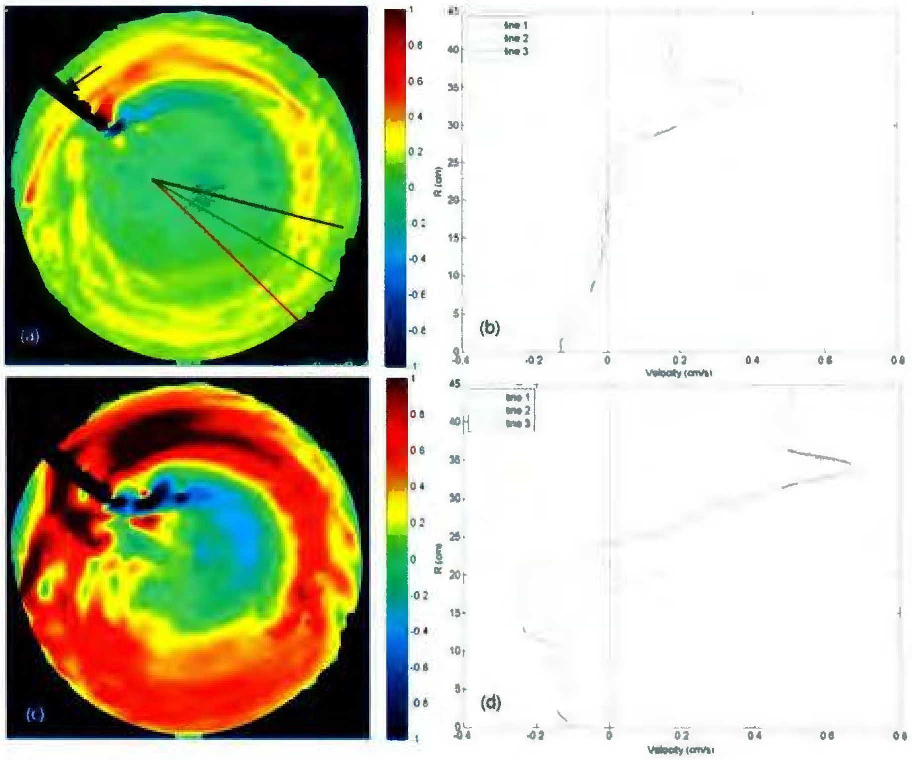

Fig.17 Azimuthal velocity of background flow measured in Experiment D1 (3.5 Volt) and in H1 (4.3 Volt). The color scale shows azimuthal velocity in cm/s. Fig. (b, d) shows their profiles measured along lines shown in (a). Sink is indicated by the arrow.

Armi (1988) studied the eastward-flowing zonal currents created by a sink on a thin rotating shell, and provided a scientific analogy between the open channel flow and zonal current on the β-plane. For the zonal current, the flow in the vicinity of the sink is narrow and rapid. The flow then slows down and spreads as it propagates far from the sink to the west. The hydraulic theory shows that the eastward flow generated by a sink is supercritical in the vicinity of the sink and subcritical farther upstream. Similar to the role of the Froude number, a main control parameter Froude/Rossby number is found to relate inertiaal forces to pressure forces arising from the width variations of a zonal current. The dimensionless Froude/Rossby number is defined as $Ro_\beta = U_{east}/(\alpha'\beta a^2)$, where U_{east} is the maximum velocity of the eastward zonal current, the coefficient α' is determined by the shape of the velocity profile and is $\alpha' = 0.25$ for a parabolic profile, a is the half-width of current, and β is the variation of the Coriolis parameter. Here, we take $\beta = 0.11\ \mathrm{rad/s}$ as a reasonable value at the half radius of the tank. This is also the location of the sink and the heater. For hydraulic zonal flows, a control is established at the location where the flow is narrow with $Ro_\beta = 1$. The flow will become subcritical with $Ro_\beta < 1$ somewhere upstream (west of the control section). When the flow is subcritical, the Rossby waves are fast enough to propagate westward and carry information from the control section. Note that all the zonal westward flows are subcritical. The theory given by Armi (1989) shows the relation between the peak velocity U_{east} and the volume flux V in an eastward zonal flow on a β-plane, such as

$$U_{east} = 0.52\beta^{1/3}V^{2/3}. \tag{3.9}$$

Here, the volume flux V is defined as

$$V = \int_{-\mathrm{a}}^{a} u(y)\mathrm{d}y, \tag{3.10}$$

where $u(y)$ is the velocity profile of zonal currents in the local Cartesian coordinates (x, y) with the origin on the axis of the zonal flow. Experimental results obtained by Armi (1989) showed appropriate experiments to check the consistency of our results with the theory. For our measurements, the velocity $u(y)$ was measured along a radius (line 4 in Fig. 19) drawn sufficiently close to the sink such that $Ro_{\beta} \approx 1$ at this particular cross section. Note that the location of the line was different in each experiment, such as the two black lines in Fig. 18 (a, b). The calculated Ro_{β} and other measurements of each experiment are listed in Table (4). The results of Exp. B1 and H1 are shown in Fig. 18. Note that only the eastward currents due to the sink were taken into account in these measurements. For that reason, the eastward currents due to the source, which can be distinguished as the second peak southward of the first peak in the velocity profiles, was excluded. These results are summarized in Fig. 19 where the peak velocity U_{east} is plotted as a function of $\beta^{1/3}V^{2/3}$. Here, the solid line shows the theoretical relation (3.9) by Armi (1989), which is in agreement with our laboratory data (line 4, shown by circles). The data is also obtained along the radius at 3 o'clock, east of the heater where the values of the Froude/Rossby number below unity, and range between 0.08 and 0.25 (See Table 4). Here, the flow is subcritical as expected. Note that the volume transport in the eastward current upstream of the control section decreases with distance from the sink because of the recirculation due to Ekman pumping/suction at a lower layer. This is also to lesser extent due to the lateral exchange with the westward current in the north.

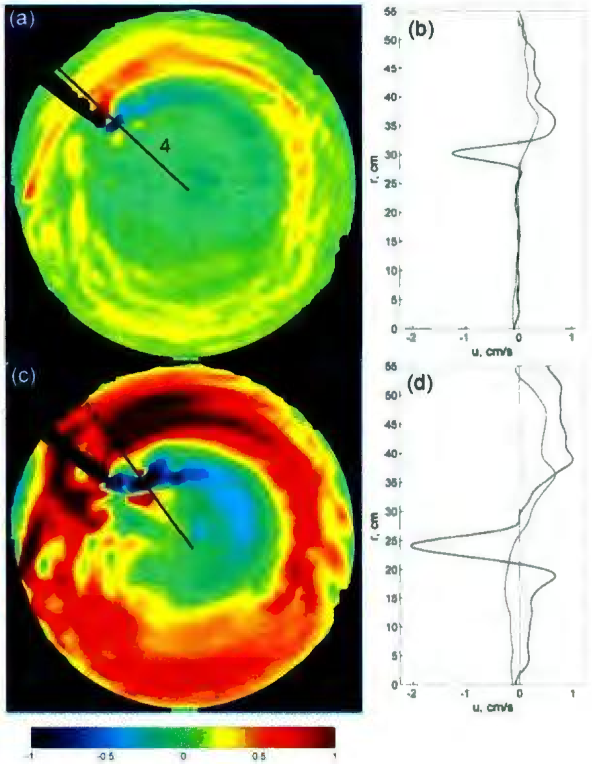

Fig.18: Azimuthal velocity of the flows created by a sink in experiments B1 (a, b) and H1 (c, d). The color scale shows azimuthal velocity in cm/s. Positive (negative) velocity corresponds to eastward (westward) flow. Profiles in (b) and (d) are measured along the radial line 4 in (a) and (c), and the line 3 in Fig. 17 (a). Solid black lines in (b, d) are profiles measured along the radial line in the vicinity of the source while the gray lines are profiles measured along the line at the east edge of the heater.

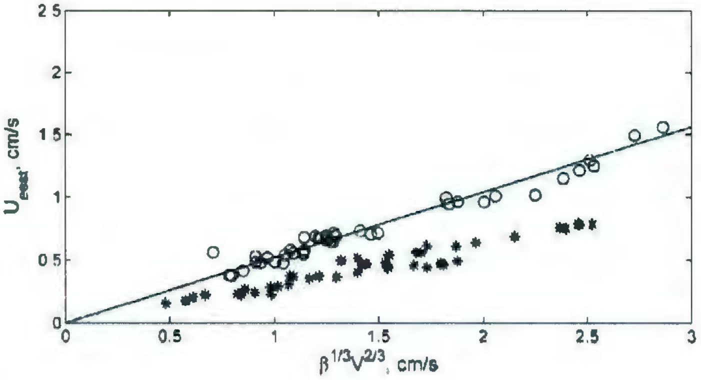

Fig.19: The peak velocity of the eastward zonal current created by the sink as a function of $\beta^{1/3}V^{2/3}$. Circles show the velocity measured in the vicinity of the sink where $Ro_\beta \approx 1$. Crosses show the velocity measured near the east edge of the heater. The solid straight line has a slope of 0.52 as the theoretical result equation (3.9).

3.5 Localized convection in a zonal jet

As shown in section 3.2, after starting the heat source, upward propagating vortices were generated; and then the warm water lens moved far from the heater due to the expansion and the baroclinic vortices. Later, the lens stretched to the west by β-plume from the region about the source. However, the situation is more complicated under a zonal background flow. In this section, a series of experiments of β-plumes developing in a zonal eastward jet are discussed.

After the zonal background flow due to the sink was well-formed and stationary, the heater was switched on. An eastward transport due to the sink and a westward β-plume due to the heater competed with each other in our experiments. The peak velocity U_{east} of the background jet was measured for each experiment as a reference (see Table 3). Here, U_{east} was measured at the eastern boundary of the heater (line 3 in Fig. 17). Two sequences of AIV images of the flow in Fig. 20 show two extremes: When the heater overwhelms the sink (the rate $\frac{W_v}{U_{east}}$ is high), the flows were still in shapes of β-plumes propagating westward (Fig.20 a-c and Fig. 9); when the strength of the sink gradually increased or when the intensity of the heater gradually decreased, and both eastward and westward transport are observed in an intermediate cases. On the contrary, if the sink was stronger (the rate $\frac{W_v}{U_{east}}$ is low), the β-plume would not form, and warm water rising to the surface above the heater would be carried to the east by the zonal background flow (Fig.20 d-f).

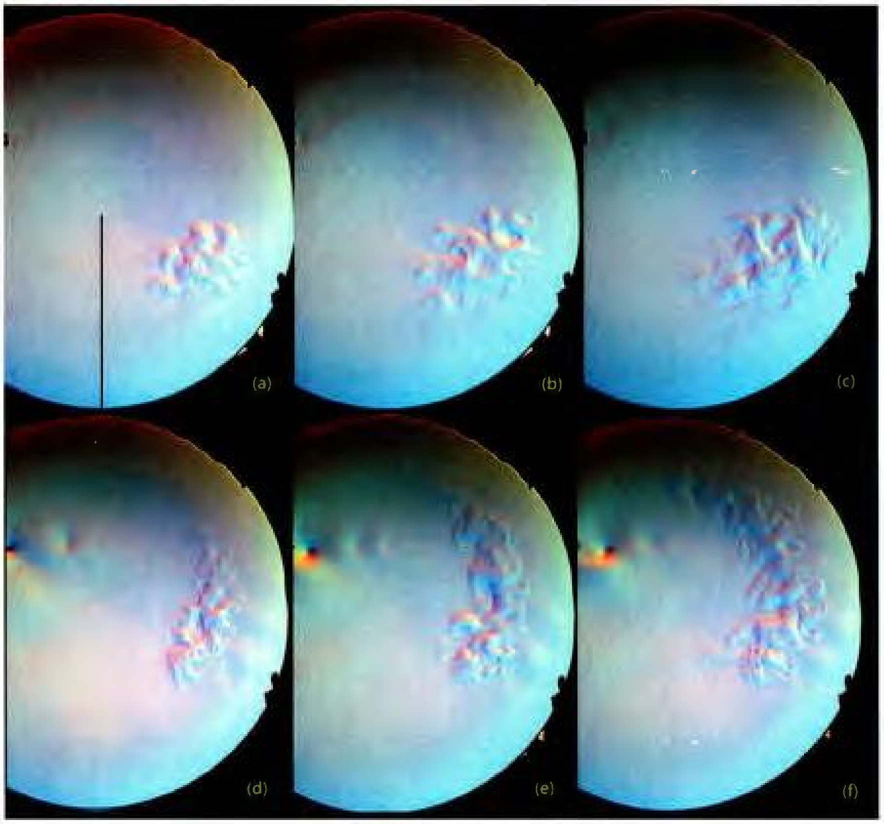

Fig.20: The evolution of the flow generated by the heater with a weak eastward background flow (a, b, c) in experiment B1 and with a strong eastward background flow (d, e, f) in experiment H1. The images were captured at times t=80s (a, d), 120s (b, e) and 160s (c, f). (For experiment B1, a peak velocity of 0.15 cm/s for the zonal background flow was measured at west edge of the heater. For experiment H1, 0.69cm/s for peak velocity of zonal background flow was measured at west edge of the heater.)

In order to find the boundary between the two regimes, we plot the distribution of the westward-propagating velocity U_{plume} of the β-plumes as a function of two parameters, the vertical velocity W_v and the peak velocity of the eastward background flow U_{east}. Here, U_{east} was measured at the eastern boundary of the heater (as black line in Fig. 16), and W_v was calculated as Eq. (1.6) (see Table 2). The mean of the westward-propagating speed of the plume, U_{plume} (see Table 3) was obtained by measuring the time it takes for the plume front to reach a radius at 6 o'clock (black line in Fig.19 (a) which is 60 degrees west of the heater). In some experiments, the distribution of the velocity U_{plume} is showing as "-", which means the plume only propagated to the east by the background jet, or could not reach 6 o'clock during the experiment (we have 400 seconds video for each experiment). Note that it was sometimes difficult to separate the β-plume due to the heater from the westward transport due to the background zonal current. This uncertainty was greater when the sink, or the zonal current, was stronger. The values of U_{plume} measured in each experiment for particular values of w and U_{east} (indicated in Fig. 21 by crosses) were interpolated into a regular grid in the plane (W_v, U_{east}) and showed as a contour plot. As one might expect, Fig. 21 shows that there is no westward propagation when the sink is relatively strong and the heater is relatively weak.

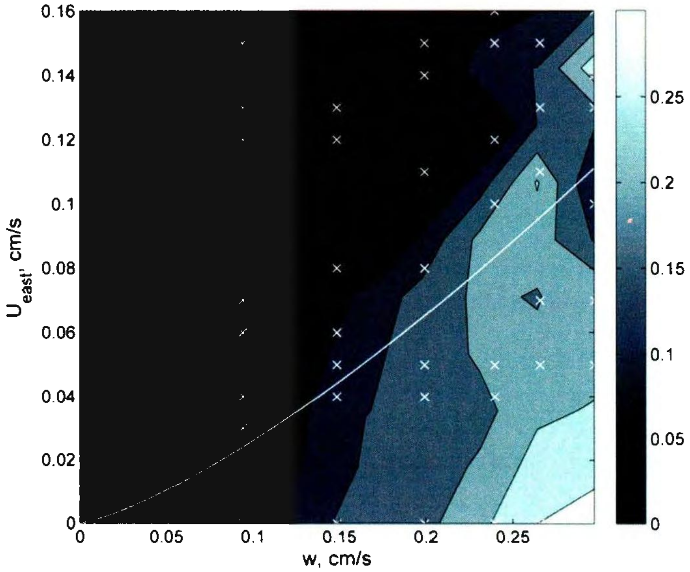

Fig.21 Contour of U_{plume} with different values of W_v and U_{east}. The gray scale shows the values of U_{plume} normalized by the zonally Rossby waves speed of meridional extent equal to the heater's diameter, $c_{gx} = \beta(r_h/\pi)^2$. Crosses indicate the values of U_{east} and W_v for each experiment where U_{plume} was measured. The white line is based on equation (3.13) and shows an estimate of the boundary between the two regimes.

Some insight into the dynamics of a β-plume in the eastward stream can be obtained by considering the propagation of Rossby waves. The plume is formed by long Rossby waves propagating upstream of the eastward zonal current. The frequency of barotropic Rossby waves, ω, is given by the dispersion relation:

$$\omega = \bar{u}k - \frac{\beta k}{k^2 + l^2 + 1/R_b^2}, \tag{3.11}$$

where $\bar{u}$ is mean zonal velocity, k and l are respectively the wavenumbers in x and y directions, and $R_b = (gh)^{1/2}$ is the barotropic radius of deformation. The x-component of the group velocity for the zonally elongated ($k \approx 0$) Rossby waves is given by

$$c_{gx} = \bar{u} - \frac{\beta}{l^2 + 1/R_b^2}, \tag{3.12}$$

while the y-component of the group velocity vanishes. Thus, when the meridional wavelength of the waves is large enough, the waves are able to overcome the zonal flow and travel westward. In our experiments, barotropic Rossby waves are emitted by baroclinic eddies above the heater. Assuming that the size of these eddies and hence the meridional wavelength of the emitted Rossby waves is determined by the baroclinic radius of deformation $R_c = (g'h_1)^{1/2}/f_0$, where g' is the reduced gravity that can be calculated in an empirical way and h_1 is the thickness of the upper layer. A critical velocity for the zonal flow can then be estimated as:

$$\bar{u} = \frac{\beta}{1/R_c^2 + 1/R_b^2}. \tag{3.13}$$

Here $g' \approx 25(B_0 r_h)^{\frac{2}{3}}/h$ is given by Maxworthy and Narimousa (1994), and $h_1 = 0.5h$ is the upper expansion layer as discussed in section 3.2. The solid line in Fig. 21 shows Eq. (3.13), which gives a reasonable estimate of the boundary between the two regimes such as $\bar{u} = U_{east}$. The critical zonal velocity is perhaps overestimated because the actual velocity of the zonal flow west of the heater is less than the peak velocity U_{east} measured at the eastern edge of the heater.

The velocity of the moving water parcels at the eastern boundary of the heater (around the black line in Fig. 16) was plotted as a function of peak velocity in background flows U_{east} in the same position and intensity of the heater (Fig. 22). Here, the velocity of the water parcel is measured by tracking the water parcels. Several clear bubbles on the surface or the distinct vortex were selected in consecutive images as conservative tracers. Their displacement with time was measured. In this way, the velocity of the water parcel can be calculated. At the eastern boundary of the heat source, the water parcels transported to the east due to the expansion of the warm water and the eastward background flow. The overall shape of Fig. 22 shows that the eastward velocity of the water parcels was proportional to the peak velocity of the background flow. This means the background flow is the main reason for the eastward flow. The red lines show a linear fit. Note that when the intensities of the background flows are approximately the same (the values of x-axis are approximately the same), the water parcels with the stronger heater power moved faster than those with the weaker heater power. The intensity of the heater can also affect the velocity of the water parcels.

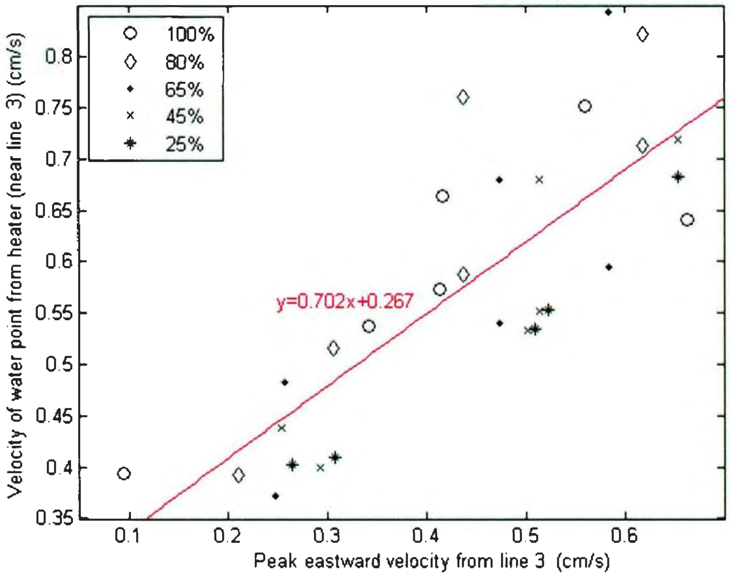

Fig.23: The relationship between the velocity of water parcel near line 3 (Fig.4 (a)) and peak velocity in the background flow (line 3) driven by the heater with various intensity: 100%, 80%, 65%, 45% and 25% (from top to bottom). The red line is one-dimensional linear interpolation.

Chapter 4: Modeling Results and Analyses

4.1 Introduction

Numerical simulations of the β-plumes were obtained by Massachusetts Institute of Technology general circulation model (MITgcm). The MITgcm has the non-hydrostatic capabilities, which can be used to simulate various hydrodynamic fluid phenomena and mixing processes over a wide range of temporal scales (Marshall et al., 1997). In our study, MITgcm is chosen for its non-hydrostatic capability (Marshall et al., 1997). The model setups are similar to that in the laboratory experiments. The main parameters of our numerical simulations are summarized in Table 7. In this chapter, the setups and the results of our numerical simulations will be given.

4.2 Model configuration and setup

Grid

The main numerical experiments were performed on the Atlantic Computational Excellence Network (ACEnet). Each experiment was performed by parallel computing with 10 numerical cores. The incompressible Navier-Stokes equations were solved on Cartesian grid with 30 vertical levels in z-coordinate and 200 × 200 cells on the horizontal coordinate. The total number of cells is 1.2×10^6. The length scale for each dimension of the cubic cell is 0.5 cm. A series of additional simulations of higher spatial resolution were performed by 40 numerical cores. That model domain has 30 z-coordinate vertical levels and 400 × 400 cells on the horizontal plane.

Boundary condition

The model domain is circled by a free-slip lateral boundary such that a cylinder with a radius $r = 50\ cm$. Therefore, a circular tank with diameter $D_n = 100\ cm$ filled with water to depth $H_n = 15$ cm is obtained by this setup. The bottom topography of our model is a no-slip boundary and is a down-open paraboloid described by $h(r) = A - Br^2$. This setup is to imitate our laboratory experiment which has a flat bottom and an up-open paraboloidal free surface as described in section 2.2. In terms of potential vorticity conservation in quasigeostrophic flow, this false bottom topography creates the beta effect in our numerical experiments. Different bottom topography is employed under the different rotation rate. For example, when the background anti-clockwise rotation is $\Omega^2 = 2.5\ \mathrm{rad}/s^{-1}$, the bottom topography is described by $h(r) = A - Br^2$, where $A = H_0 - \frac{\Omega^2 R^2}{4g} - 6\ cm$, and $B = \frac{\Omega^2}{2g} = 3.1 \times 10^{-3}\ cm^{-1}$. Here, A and B is calculated by the formula (2.1), H_0 is the mean depth of the rotating fluid, Ω is the rotation rate of the tank, R is the radius of the tank, and g is the gravitational acceleration. The depth of the fluid varies from $h(0) = 6\ cm$ to $h(R) = 14\ cm$ and makes the mean water depth in the tank is $\frac{h(R)+h(0)}{2} = 10\ cm$ (See Fig. 24). These setups make the water depth variation the same as that in our previous laboratory expeiermnts.

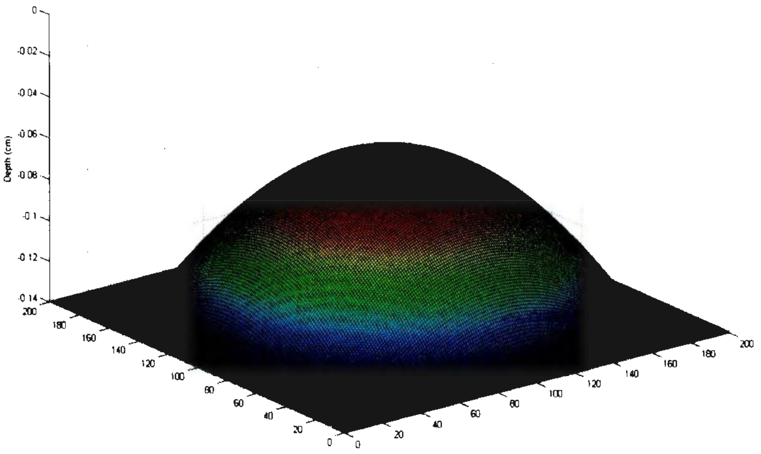

Fig. 23 The bottom topography of our model when the background anti-clockwise rotation rate of the domain is 2.5 rad/s^{-1}.

Heat Source

As in our laboratory experiments, a disk-shape heater is induced to generate the flows in our numerical experiments. The radius and the thickness of the heater are 7 cm and 0.5 cm (1 cell) respectively. The center of the heater locates at 4 o'clock, radius $r = 27\ cm$, and 5 cm below the surface. In some experiments, the heater is located at either deeper or shallower layer (See Table 7). The heat flux of the heater in most cases is $5\ W/cm^2$. In a number of simulations, the heat flux is varied from $1\ W/cm^2$ to $10\ W/cm^2$. All there setups are to approximate the heating system in our laboratory experiments.

4.3 Results of numerical simulations

A typical evolution of the flow in the simulation S9 is shown by a sequence of images (Fig. 24) of relative vorticity, $\xi = \mathrm{curl}(V_h)$, where $V_h$is the horizontal velocity. These images show some similar features to our laboratory results. As Fig.24 shows, the warm upwelling water was generated from the heater in a short time after turning on the heater. A clear frontal jet flowing clockwise was formed due to the warm water divergence at the surface. The associated vorticity field shows both cyclones (red) and anticyclones (blue) are as obvious as those in laboratory results. The cyclones are likely due to the local downwelling of relatively cool water at the surface. The insert of Fig.24 (a) shows the vertical velocity of the source region in the upper layer (vertically averaged from layer 2 to 4 and also averaged over 3 measurements from level 2 to level 4). As expected, both upward-propagating and downward-propagating can be observed. The maximum value of the upwelling velocity 0.25 cm/s corresponds to our calculated laboratory upward-propagating speed in equation (3.3). At the same time, a baroclinic region was formed above the heater and emitted Rossby waves. Afterwards, this region expands both westward and eastward. However, in the following period, an additional transport to the west can be observed (Fig. 24 (b-d). These westward plumes which shows the "pathways" of the warm water were established by the Rossby waves. Note that the typical Rossby number $Ro = |\xi|/f_0$ is clearly below unity. For example, in experiment S9, the maximum value of the Rossby number is about 0.2. It is necessary to compare the numerically simulated flows with the laboratory flows. Fig. 25 shows the color maps of the azimuthal velocity for laboratory experiment A4 and simulation S9 at different times. In spite of the different developing speed of the β-plumes, the numerical simulations reproduced general features of the laboratory experiments. Two distinctive β-plumes consisting of two jets flowing in the opposite directions can be observed in Fig. 25 (d).

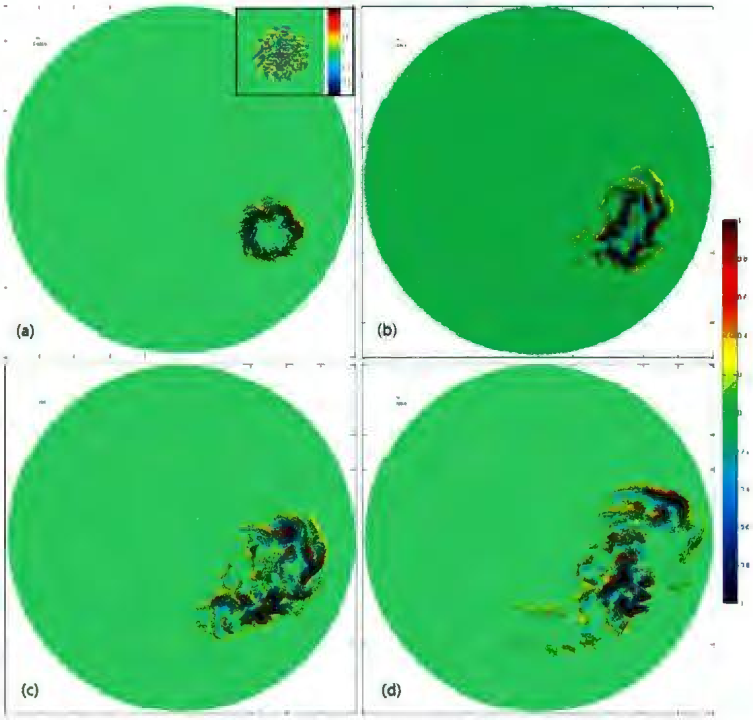

Fig. 24 Sequence of relative vorticity field at the surface of the fluid layer from the numerical simulation S9 in Table 7 for times t = 60 s (a), 200 s (b), 400 s (c), and 800 s (d). The color scale show the vorticity in s^{-1}. The color insert in (a) shows the vertical velocity of the source region.

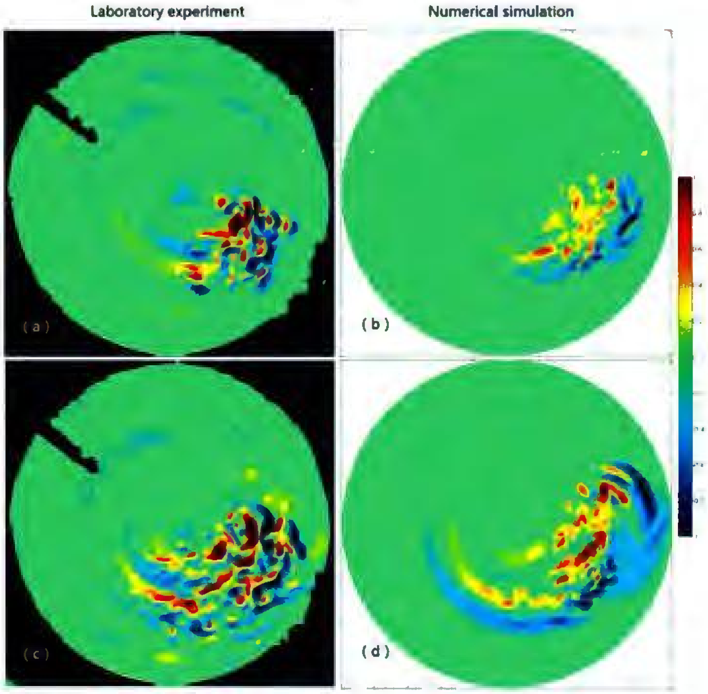

Fig. 25 Comparison of the azimuthal velocity fields in laboratory experiment A4 (a) and (c) and numerical simulation S9 (b) and (d): t=140s (a), 320 (c), t=400 (b) and 800 (d). Color scale shows velocity in cm/s. Yellow-read indicate eastward jets while blue indicates westward jets.

Chapter 5: Conclusion

In this thesis, the laboratorial and numerical model of β-plumes were introduced. In laboratorial experiments, we have shown some potential mechanisms involved in the GWS phenomenon. A heater was fixed at the bottom of a rotating tank to create the warm upwelling water. It is the buoyancy source. After the heater was started, the baroclinic eddies emitted barotropic Rossby waves and established β-plume propagating to the west. Then zonal eastward background flow was generated by a sink, which affected the β-plume as the eastward wind on Saturn.

The first series of the laboratory experiments was designed to study the flows generated by the buoyancy source on the *f*-plane. With the visualized results by the AIV method, we first described the flows created by a buoyancy source, and showed that the area of the lens changes as a function of the strength of the buoyancy source in the initial period. In addition, a simple β-plume was demonstrated as a reference point for further experiments. The feature of a β-plume showed that both components of velocity in the β-plume were proportional to the intensity of the buoyancy source. In the numerical simulation, the β-plumes were also observed and showing some similar features to our laboratory results. In the second series of the laboratory experiments, the background flow in the form of an eastward zonal current was present to show that a β-plume can be overwhelmed by the eastward current such that the warm water upwelled to the surface above the heater was advected to the east. Here, we considered the barotropic Rossby waves emitted by the baroclinic eddies and acquired a regime diagram showing the area where the β-plume could exist. In this diagram, the control parameters were the buoyancy flux of the heater and the velocity of the zonal flow. In the second series of experiments, we also demonstrated a linear relationship between the peak velocity in the zonal current due to a sink and the volume flux on the place where the zonal current was supercritical.

Assuming that the β-plume was generated by the upwelling source in the GWS on Saturn, we calculate the Rossby wave speed emitted by the storm. Let us take the radius of the storm to be approximately $R_s = 2500\ \mathrm{km}$ and assume the radius of deformation is of similar magnitude $R_b = 2500\ \mathrm{km}$ (see Read et al. 2012). Further we take the meridional wavelength of the Rossby wave equals to 4 R_s, the group velocity c_{gx} of zonal Rossby waves can be estimated to be

$$c_{gx} = \frac{\beta}{\left(\frac{2\pi}{4R_s}\right)^2 + \left(\frac{1}{R_b}\right)^2} \approx 9\ \mathrm{m/s}\,.$$

This result is in agreement with the measured moving rate of the storm head of the GWS which was 10 m/s faster than the peak westward zonal wind (see Section 1.1). Considering the influences of the strong zonal wind on the Saturn, the circulation inside the β-plume may not be observed. We can expect the storm tails which transported eastward by the zonal wind on Saturn are similar to what happed in our experiments with strong eastward background flows.

References

A. C. B. Aguiar, P. L. Read, R. D. Wordsworth, T. Salter, Y. H. Yamazaki, "A laboratory model of Saturn's North Polar Hexagon," Icarus **206**(2), 755, DOI:10.1016/j.icarus.2009.10.022 (2010).

A. E. Gill, "Atmosphere-Ocean Dynamics", Academic Press, San Diego, **30** (1982).

A. G. Slavin, and Y.D. Afanasyev, "Multiple zonal jets on the polar beta plane," Phys Fluids **24**, 016603, DOI: 10.1063/1.3678017 (2012).

A. Sanchez-Lavega, T. del Rio-Gaztelurrutia, and R. Hueso, "Deep winds beneath Saturn's upper clouds from a seasonal long-lived planetary-scale storm," Nature **475**, 71, doi:10.1038/nature10203 (2011).

D. L. Volkov, L. L. Fu, "On the Reasons for the Formation and Variability of the Azores Current," J. Phys. Oceanogr. **40** (2197), DOI: 10.1175/2010JPO4326.1 (2010).

G. Anitha, M. Ravichandran, and R. Sayanna, "Surface buoyancy flux in Bay of Bengal and Arabian Sea," Annales Geop. **26**, 395–400, (2008).

G. Fischer, W. S. Kurth, D. A. Gurnett, P. Zarka, U. A. Dyudina, A. P. Ingersoll, S. P. Ewald, C. C. Porco, A. Wesley, C. Go, and M. Delcroix, "A giant thunderstorm on Saturn," Nature **475**, 75, DOI: 10.1038/nature10205 (2011).

J. O. Shin, S. B. Dalziel and P. F. Linden, "Gravity currents produced by lock exchange," J. Fluid Mech. **521**, 1, DOI:10.1017/S002211.2004.00165X (2004).

H. J. S. Fernando, R.-R. Chen, and D. L. Boyer, "Effects of rotation on convective turbulence," J. Fluid Mech, **228**(513) (1991).

H. M. Stommel, "Is the South Pacific helium-3 plume dynamically active?," Earth Planet. Sci. Lett. **61**, 63 (1982).

L. Armi, "Hydraulic control of zonal currents on a β-plane," J. Fluid Mech. **201**, 357 (1989).

M. A. Spall, R. S. Pickart, "Wind-Driven Recirculations and Exchange in the Labrador and Irminger Seas," J. Phys. Oceanogr., **33**. 1819-1845 (2003)

M. F. Cronin, J. Sprintall, "Upper Ocean Structure: Wind and Buoyancy-forced Upper Ocean," Encyclopedia of Ocean Sciences, DOI:10.1006/rwos.2001.0157 (2001)

M. K. Davey, and P. D. Killworth, “Flows produced by discrete sources of buoyancy,” J. Phys. Ocean. **19**, 1279 (1989).

M.S. Tiscareno, J.A. Burns, P.D. Nicholson, M.M. Hedman, C.C. Porco, “Cassini imaging of Saturn’s rings II: A wavelet technique for analysis of density waves and other radial structure in the rings”, Icarus **189.** 14-34 (2007)

Peter Read, “Storm-clouds brooding on towering heights,” Nature 475(44), DOI:10.1038/475044a (2011)

P. Read, T. E. Dowling, and G. Schubert, “Saturn’s rotation period from its atmospheric planetary-wave configuration,” Nature 460(608), (2009)

P. L. Read, B. J. Conrath, L. N. Fletcher, P. J. Gierasch, A. A. Simon-Miller and L. C. Zuchowski, “Mapping potential vorticity dynamics on saturn: Zonal mean circulation from Cassini and Voyager data,” Planet. Space Sci. 57(14), 1682, DOI:10.1016/j.pss.2009.03.004 (2009).

R. Grothahn, “Baroclinic instability,” Elsevier Science Ltd. Rwas.2002.0076, DOI:10.1006/rwas.2002.0076 (2002).

R. W. Griffiths and P. F. Linden, “The stability of buoyancy driven coastal currents,” Dyn. Atmos. Oceans, 5(281) (1994).

T. B. Benjamin, “Gravity currents and related phenomena,” J. Fluid Mech. **31**, 209 (1968).

T. M. Özgökmen, Eric P. C Hassignet, Claes G. H. Rooth, “On the Connection between the Mediterranean Outflow and the Azores Current,” Journal of Physical Oceanography **31**(461) (2001).

T. Maxworthy, and S. Narimousa, “Unsteady, turbulent convection into a homogeneous, rotating fluid, with oceanographic applications,” J. Phys. Oceanogr. **24**, 865 (1994).

Y. D. Afanasyev, P. B. Rhines, and E. G. Lindahl, “Velocity and potential vorticity fields measured by altimetric imaging velocimetry in the rotating fluid,” Exp. Fluids 47, 913, DOI: 10.1017/S0022112089000972 (2009).

Y. D. Afanasyev, S. O’Leary, P. B. Rhines, and E. G. Lindahl, “On the origin of jets in the ocean,” Geoph. Astroph. Fluid Dyn. **106**(2), 113 DOI: 10.1080/03091929.2011.562896 (2011).

Y. D. Afanasyev and Y. Sui, “Buoyancy storms in a zonal stream on the polar beta-plane: experiments with altimetry,” Phys. Of Fluids. In press, arXiv:1304.3325 (2013)

Appendix

Table 1: Measurements of the Supplemental Experiment.

Image ID of Fig. 6	Temperature (°C)	Density ρ (kg/m^3)	density difference $\Delta\rho(g/cm^3)$	Baroclinic radius of deformation (cm)
a	20.2	998.182	0	0
b	30.6	995.462	2.72	1.03
c	33.9	994.402	3.78	1.22
d	38.1	992.925	5.257	1.44

Table 2: Date of Upwelling Flows

Q_h *(J/s)*	F (cm^4/s^3)	B_0 (cm^2/s^3)	Z_t (cm)	Z_m (cm)	W_v (cm/s)	Q_m (cm^3/s)
1000	60	0.39	0.33	0.73	0.28	43.1
800	48	0.31	0.30	0.64	0.25	38.5
650	39	0.24	0.26	0.57	0.23	35.2
450	27	0.18	0.23	0.49	0.19	29.3
250	15	0.10	0.16	0.37	0.15	21.6

Q_h: Heat flux of the heater

F: Buoyancy flux of heater

B_0: Buoyancy flux per unit area

Z_t: The depth of the 3D turbulent layer

Z_m: Transition depth

W_v: Upward speed of propagating of the warm water (quasi-2D vortices)

Q_m: Mass flux of the upwelling water

Table 3: Measurements of Experiments

Experiment ID	Heater intensity (Watt)	Buoyancy flux ($\mathrm{cm}^4/\mathrm{s}^3$)	Pump voltage (volt)	Peak eastward velocity of the background jet along line 3 (cm/s)	Peak westward velocity of the background jet along line 3 (cm/s)	Angular speed of the westward plume (rad/s)
A1	1000	60	0	0	0	0.0038
A2	800	48	0	0	0	0.0036
A3	650	39	0	0	0	0.0030
A4	450	27	0	0	0	0.0022
A5	250	15	0	0	0	0.0019
A6	100	6	0	0	0	-
B1	1000	60	3	0.15	-0.14	0.0035
B2	800	48	3	0.17	-0.13	0.0031
B3	650	39	3	0.21	-0.15	0.0027
B4	450	27	3	0.24	-0.08	0.0020
B5	250	15	3	0.23	-0.12	-
B6	100	6	3	0.22	-0.12	-
C1	1000	60	3.3	0.30	-0.07	0.0030
C2	800	48	3.3	0.27	-0.11	0.0031
C3	650	39	3.3	0.23	-0.1	0.0027
C4	450	27	3.3	0.23	-0.05	0.0020
C5	250	15	3.3	0.29	-0.06	0.0017
C6	100	6	3.3	0.29	-0.06	-
D1	1000	60	3.5	0.38	-0.05	0.0028
D2	800	48	3.5	0.39	-0.05	0.0026

D3	650	39	3.5	0.43	-0.05	0.0026
D4	450	27	3.5	0.45	-0.04	0.0017
D5	250	15	3.5	0.45	-0.04	0.0017
D6	100	6	3.5	0.44	-0.03	-
E1	1000	60	3.8	0.54	-0.05	0.0026
E2	800	48	3.8	0.55	-0.07	0.0023
E3	650	39	3.8	0.55	-0.04	0.0022
E4	450	27	3.8	0.61	-0.04	0.0020
E5	250	15	3.8	0.61	-0.05	0.0015
E6	100	6	3.8	0.56	-0.04	-
F1	1000	60	4	0.36	-0.13	0.0020
F2	800	48	4	0.37	-0.15	0.0019
F3	650	39	4	0.37	-0.16	0.0014
F4	450	27	4	0.36	-0.15	-
F5	250	15	4	0.52	-0.13	-
F6	100	6	4	0.50	-0.15	-
G1	1000	60	4.1	0.64	-0.16	0.0018
G2	800	48	4.1	0.48	-0.13	0.0014
G3	650	39	4.1	0.44	-0.16	-
G4	450	27	4.1	0.47	-0.11	-
G5	250	15	4.1	0.47	-0.08	-
G6	100	6	4.1	0.50	-0.07	-
H1	1000	60	4.3	0.69	-0.10	-
H2	800	48	4.3	0.76	-0.13	-
H3	650	39	4.3	0.75	-0.12	-
H4	450	27	4.3	0.78	-0.14	-
H5	250	15	4.3	0.77	-0.13	-
H6	100	6	4.3	0.78	-0.13	-

Table 4: The Measurements of Background zonal Jets

Experiment ID	Line 3				Line 4			
	W (cm)	V (cm^2/s)	U_{east} (cm/s)	Ro_β	W (cm)	V (cm^2/s)	U_{east} (cm/s)	Ro_β
B1	10.02	1.04	0.1560	0.2486	7.2028	2.4379	0.4128	1.2732
B2	16.04	1.36	0.1751	0.1089	7.1428	2.2149	0.376	1.1792
B3	15.70	1.49	0.2045	0.1327	9.994	1.8588	0.5619	0.9002
B4	19.93	2.69	0.2401	0.0967	8.6417	2.8078	0.478	1.0241
B5	20.31	2.34	0.2310	0.0896	7.5995	2.1706	0.3799	1.0526
B6	15.27	1.71	0.2245	0.154	7.4383	2.9602	0.5183	1.499
C1	19.62	3.44	0.3054	0.1269	8.5519	3.7813	0.564	1.2339
C2	18.07	2.47	0.2648	0.1298	7.0286	2.7028	0.5277	1.709
C3	17.81	2.40	0.2246	0.1133	7.7645	3.5495	0.5534	1.4687
C4	19.61	3.04	0.2266	0.0943	8.2106	3.1297	0.4837	1.148
C5	19.86	3.03	0.2827	0.1147	7.2227	2.7062	0.4817	1.4773
C6	19.93	3.19	0.2880	0.116	8.497	3.3172	0.4745	1.0515
D1	20.8	4.17	0.3715	0.1369	8.5109	4.3427	0.692	1.5286
D2	21.6	5.16	0.4012	0.1373	8.8551	3.3543	0.5409	1.1038
D3	22.7	5.99	0.4373	0.1357	9.4467	4.3822	0.663	1.1888
D4	21.2	5.39	0.4701	0.1666	8.9027	3.8156	0.5775	1.1658
D5	22.7	5.91	0.4791	0.148	8.728	4.5243	0.6472	1.3593
D6	21.4	5.27	0.4581	0.159	8.1821	4.1495	0.6702	1.6017
E1	22.6	6.02	0.5365	0.1676	9.4472	4.3514	0.6607	1.1844
E2	23.0	6.80	0.5607	0.1689	9.1993	3.7856	0.5467	1.0337
E3	22.10	6.01	0.5440	0.1782	8.4328	4.5502	0.7155	1.6098
E4	23.23	7.11	0.6141	0.1821	9.9481	5.5144	0.7048	1.1394

E5	23.86	7.97	0.6093	0.1712	8.3665	3.4816	0.581	1.3281
E6	23.44	6.93	0.5568	0.1621	9.6268	5.2284	0.7333	1.266
F1	19.88	3.94	0.3549	0.1437	10.2403	4.2142	0.6734	1.0275
F2	19.10	3.47	0.3745	0.1642	8.9267	3.8062	0.6797	1.3647
F3	19.15	3.55	0.3689	0.161	10.5769	5.7115	0.715	1.0227
F4	20.24	4.61	0.3635	0.142	9.5513	4.084	0.6869	1.2048
F5	19.93	5.16	0.5157	0.2077	9.5017	4.5901	0.6941	1.2302
F6	19.77	4.73	0.4950	0.2026	9.6948	4.4644	0.6494	1.1056
G1	24.37	8.58	0.6403	0.1725	14.6873	15.0788	1.5572	1.155
G2	23.34	6.72	0.4588	0.1348	11.6267	7.6688	0.9952	1.1779
G3	23.86	7.11	0.4433	0.1246	11.6332	8.8425	0.9617	1.137
G4	24.99	7.58	0.4624	0.1185	12.7321	10.5125	1.0161	1.0029
G5	24.43	7.52	0.4727	0.1267	12.1311	8.0114	0.963	1.047
G6	25.30	8.00	0.4913	0.1228	10.831	7.7465	0.9457	1.2898
H1	23.70	9.83	0.6874	0.1958	12.6346	9.2052	1.0104	1.0127
H2	25.05	11.36	0.7583	0.1934	12.3547	12.4098	1.2935	1.3559
H3	25.15	11.57	0.7516	0.1901	14.3837	14.0329	1.491	1.153
H4	23.34	12.50	0.7827	0.2299	13.1936	11.4725	1.1492	1.0563
H5	23.34	12.05	0.7787	0.2287	13.4598	12.0428	1.2131	1.0714
H6	23.60	12.00	0.7868	0.226	13.6634	12.5545	1.2478	1.0694

W: The width of the eastward jet. For line 4, only the jets due to the sink are taken into account.

V: The volume transport of the eastward jet.

U_{east}: The value of the peak velocity of the eastward jet along line 4.

Ro_{β}: The dimensionless Froude/Rossby number of the eastward jet.

Table 5: List of the Expansion of Lens of Warm Water

Experiment ID	W_v (cm/s)	$d(r_1^2)/dt$ (cm^2/s)
A1	0.28	1.49
A2	0.25	1.22
A3	0.23	1.04
A4	0.19	0.72
A5	0.15	0.31

Table 6: Vortex Diameter

Vortex Id	D (cm)	Vortex Id	D (cm)	Vortex Id	D (cm)	Vortex Id	D (cm)	Vortex Id	D (cm)
A1 160s Vorx 1	3.0	A2 160s Vorx 1	2.8	A3 160s Vorx 1	2.5	A4 160s Vorx 1	1.5	A5 160s Vorx 1	1.1
A1 160s Vorx 2	3.2	A2 160s Vorx 2	2.6	A3 160s Vorx 2	2.4	A4 160s Vorx 2	1.6	A5 160s Vorx 2	0.8
A1 160s Vorx 3	4.1	A2 160s Vorx 3	2.4	A3 160s Vorx 3	1.9	A4 160s Vorx 3	1.2	A5 160s Vorx 3	0.9
A1 180s Vorx 1	3.0	A2 180s Vorx 3	2.5	A3 180s Vorx 1	2.4	A4 160s Vorx 1	1.5	A5 180s Vorx 1	1.0
A1 180s Vorx 2	2.8	A2 180s Vorx 2	2.4	A3 180s Vorx 2	2.3	A4 180s Vorx 2	1.6	A5 180s Vorx 2	0.8
A1 180s Vorx 3	3.3	A2 180s Vorx 3	2.8	A3 180s Vorx 3	2.4	A4 180s Vorx 3	1.5	A5 180s Vorx 3	1.1
A1 200s Vorx 1	3.4	A2 200s Vorx 1	2.6	A3 200s Vorx 1	2.6	A4 180s Vorx 1	1.6	A5 200s Vorx 1	0.9
A1 200s Vorx 2	3.6	A2 200s Vorx 2	2.8	A3 200s Vorx 2	2.1	A4 200s Vorx 2	1.3	A5 200s Vorx 2	1.1
A1 200s Vorx 3	2.9	A2 200s Vorx 3	3.1	A3 200s Vorx 3	2.1	A4 200s Vorx 3	1.6	A5 200s Vorx 3	1.1
A1 220s Vorx 1	3.3	A2 220s Vorx 3	3.0	A3 220s Vorx 1	2.2	A4 200s Vorx 1	1.5	A5 220s Vorx 1	1.0
A1 220s Vorx 2	3.1	A2 220s Vorx 3	3.2	A3 220s Vorx 2	2.7	A4 220s Vorx 2	1.5	A5 220s Vorx 2	0.9
A1 220s Vorx 3	4.2	A2 220s Vorx 3	2.9	A3 220s Vorx 3	2.1	A4 220s Vorx 3	2.0	A5 220s Vorx 3	1.2

D: the diameter of the Vortex

Table 7: Numerical Experiment

Experiment ID	Q, W/cm^2	Ω, $rads^{-1}$	L	vh, cm^2s^{-1}	vz, cm^2s^{-1}	α, $(°C)^{-1}$
S1	1	2.5	5	10^{-2}	10^{-2}	2×10^{-4}
S2	10	2.5	5	10^{-2}	10^{-2}	2×10^{-4}
S3	5	2.5	5	10^{-2}	10^{-2}	2×10^{-4}
S4	5	1	5	10^{-2}	10^{-2}	2×10^{-4}
S5	5	5	5	10^{-2}	10^{-2}	2×10^{-4}
S6	5	2.5	5	10^{-2}	10^{-2}	2×10^{-4}
S7	5	2.5	5	10^{-2}	10^{-2}	2×10^{-4}
S8	5	2.5	5	10^{-2}	10^{-1}	2×10^{-4}
S9	5	2.5	5	10^{-1}	10^{-2}	2×10^{-4}
S10	5	2.5	5	10^{-1}	10^{-1}	2×10^{-4}
S11	5	2.5	5	10^{-2}	10^{-2}	4×10^{-4}
S12	5	2.5	5	10^{-2}	10^{-2}	8×10^{-4}
S13	5	2.5	3	10^{-1}	10^{-2}	8×10^{-4}
S14	5	2.5	3	10^{-1}	10^{-2}	2×10^{-4}
S15	5	2.5	3	10^{-2}	10^{-2}	2×10^{-4}
S16	5	2.5	1	10^{-1}	10^{-2}	8×10^{-4}
S17	5	2.5	1	10^{-1}	10^{-2}	2×10^{-4}
S18	5	2.5	1	10^{-2}	10^{-2}	2×10^{-4}

Q is the heat flux.

Ω is the rotation rate of the domain.

L is the level of the heater.

vh is the horizontal friction coefficient.

vz is the vertical friction coefficient.

α is the thermal expansion coefficient.